SAXS imaging reveals optimized osseointegration properties of bioengineered oriented 3D-PLGA/aCaP scaffolds in a critical size bone

Biomaterials 294 (2023) 121989

Contents lists available at ScienceDirect

Biomaterials

journal homepage: www.elsevier.com/locate/biomaterials

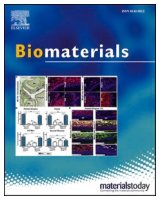

SAXS imaging reveals optimized osseointegration properties of bioengineered oriented 3D-PLGA/aCaP scaffolds in a critical size bone defect model

Elisa A. Casanova [a,1], Adrian Rodriguez-Palomo [b,1], Lisa Stähli [a], Kevin Arnke [a], Olivier Gröninger [c], Melanie Generali [d], Yvonne Neldner [a], Simon Tiziani [a], Ana Perez Dominguez [e], Manuel Guizar-Sicairos [f], Zirui Gao [f], Christian Appel [f], Leonard C. Nielsen [b], Marios Georgiadis [g], Franz E. Weber [e], Wendelin Stark [c], Hans-Christoph Pape [a], Paolo Cinelli [a,h,2,*], Marianne Liebi [b,i,2]

[a] Department of Trauma Surgery, University of Zurich, University Hospital Zurich, Zurich, Switzerland
[b] Department of Physics, Chalmers University of Technology, Gothenburg, Sweden
[c] Institute for Chemical and Bioengineering, ETH Zurich, Zurich, Switzerland
[d] Institute for Regenerative Medicine (IREM), Center for Therapy Development and Good Manufacturing Practice, University of Zurich, Zurich, Switzerland
[e] Oral Biotechnology and Bioengineering, Department of Cranio-Maxillofacial and Oral Surgery, Center for Dental Medicine, University of Zurich, Zurich, Switzerland
[f] Swiss Light Source, Paul Scherrer Institute, Villigen, Switzerland
[g] Department of Radiology, Stanford School of Medicine, Stanford, CA, USA
[h] Center for Applied Biotechnology and Molecular Medicine (CABMM), University of Zurich, Zurich, Switzerland
[i] Centre for X-ray Analytics, Swiss Federal Laboratories for Materials Science and Technology (EMPA), St. Gallen, Switzerland

ARTICLE INFO

Keywords:
Mesenchymal stromal cells
Critical size bone defect
Scaffold
PLGA/aCaP
Extracellular matrix
SAXS tomography

ABSTRACT

Healing large bone defects remains challenging in orthopedic surgery and is often associated with poor outcomes and complications. A major issue with bioengineered constructs is achieving a continuous interface between host bone and graft to enhance biological processes and mechanical stability. In this study, we have developed a new bioengineering strategy to produce oriented biocompatible 3D PLGA/aCaP nanocomposites with enhanced osseointegration. Decellularized scaffolds -containing only extracellular matrix- or scaffolds seeded with adipose-derived mesenchymal stromal cells were tested in a mouse model for critical size bone defects. In parallel to micro-CT analysis, SAXS tensor tomography and 2D scanning SAXS were employed to determine the 3D arrangement and nanostructure within the critical-sized bone. Both newly developed scaffold types, seeded with cells or decellularized, showed high osseointegration, higher bone quality, increased alignment of collagen fibers and optimal alignment and size of hydroxyapatite minerals.

1. Introduction

While bone possesses an innate capacity for regeneration and repair, the natural bone-healing process is hindered in the case of large-scale bone defects. Bone loss greater than two times the diameter of the long bone diaphysis or a defect greater than 2.5 cm is unlikely to result in union despite appropriate stabilization methods [1]. These fractures, called “critical-size” defects [2], can occur following trauma, infection, or bone tumor resections and are associated with high rates of non-union [3,4]. Loss of bone substance caused by trauma or other diseases affects more than 20 million people annually worldwide [5] and is bound to high socio-economic costs. Estimations in the United States indicate that more than half a million patients receive bone defect repairs generating a yearly financial burden greater than $2.5 billion [6]. Due to the constantly ageing population, an increased occurrence of bone disorders like bone fractures, osteoporosis, bone infection, tumors and rheumatic

* Corresponding author. Department of Trauma Surgery, University of Zurich, University Hospital Zurich, Zurich, Switzerland.
E-mail address: paolo.cinelli@usz.ch (P. Cinelli).
[1] These authors contributed equally.
[2] These senior authors contributed equally to this study.

https://doi.org/10.1016/j.biomaterials.2022.121989
Received 12 April 2022; Received in revised form 1 December 2022; Accepted 24 December 2022
Available online 2 January 2023

diseases is expected to occur in the future [7,8]. Currently, several approaches are available to stimulate or augment bone regeneration when the natural process of bone healing is insufficient. Standard treatments such as distraction osteogenesis [9], bone transport [10], different bone-grafting methods (autografts and allografts) [11], and the use of tissue-engineered bone substitutes or growth factors [12] are frequently used in the clinics [4].

The current "gold standard treatment" to reconstruct bone in the case of critical-size bone defects is autologous bone grafting [11,13]. This treatment possesses optimal osseointegration as well as osteogenic, osteoconductive, and osteoinductive properties, as the patient's tissue is used,. [11,14]. Alternatively, transplantation of autologous bone marrow aspirates together with allogenic spongiosa chips can be used [15]. However, these methods require additional surgery for harvesting the graft material, often leading to donor site pain and morbidity [16], often associated with limited availability and poor results [1,13]. Bone tissue engineering represents an appealing alternative, where there are three main requirements for successful bone tissue engineering: the selection of an adequate biomaterial, growth factors and appropriate cells [17]. The choice of the biomaterial employed is of significant importance because the scaffolds should facilitate bone cell attachment, cell proliferation and migration (osteoconductive properties) and at the same time stimulate the differentiation of osteoprogenitor cells into osteoblasts (osteoinductive properties) [18,19]. Furthermore, they should also be able to promote vascularization to guarantee the transport of nutrients and oxygen for the newly formed bone tissue [20–22]. Many efforts have been made in the past decade to develop biomimetic materials that functionally augment the native bone tissue [23–25]. However, formation of fibrous tissue often occurs at the biomaterial-tissue interface, resulting in osseointegration failure by encapsulation of the graft by fibrotic connective tissue leading to non-union and aseptic loosening. Several approaches were used to mimic isolated components of native bone, particularly the extracellular matrix (ECM), by combining synthetic fibrous materials with cell-adhesive peptide sequences and growth factors or by incorporating hydroxyapatite [26–29]. However, natural bone ECM is challenging to mimic, consisting of fibrous collagen, hydroxyapatite, proteoglycans and growth factors [30]. Decellularized bone has gained attention because the natural ECM can provide an appropriate cellular microenvironment for bone-producing cells [31], has an excellent mechanical and structural profile and lack of immunogenicity in host tissues [32]. This approach presents different technical difficulties, such as removing cells from the native bone tissue and problems with integration of the implanted decellularized bone with native bone [33].

Synthetic polymers are of interest because they allow the fabrication of scaffolds with complex shapes and adapted mechanical properties and degradation rates [7]. Poly (glycolic acid), poly (lactic acid), and especially their co-polymers (poly (DL-lactic–glycolic acid), PLGA), are commonly used polymers for the production of bone scaffolds [34–36]. PLGA is a linear copolymer with varying ratios of its monomers GA (glycolic acid) and LA (lactic acid), which offers a wide range of degradation rates [36] that can be tailored to specific needs [35,37]. Electrospun PLGA scaffolds are highly porous with interconnected pores and possess a high surface-to-volume ratio [38]. This favours adhesion, proliferation, migration and differentiation of endogenous and scaffold-seeded bone cells and facilitates vascularization and exchange of nutrients and metabolic waste [38,39]. The morphology of the electrospun fibres can be controlled by collecting them in a static plate [38] (random) or in a rotating drum [40,41] (aligned). It was shown that cells' spreading and migrating are guided by the nanofibers' orientation [39,40,42], as demonstrated by Lee and co-workers in human ligament fibroblasts [43]. Similarly, using aligned nanofibers for bone scaffolds could lead to the alignment of osteoblasts and the generation of an oriented ECM (similar to the native ECM), which could further enhance endogenous cell migration.

Although PLGA is biocompatible, it possesses poor osteoconductivity, and suboptimal mechanical properties for load-bearing applications as in tissue engineering [35,37]. Composite PLGA scaffolds in combination with amorphous calcium-phosphates nanoparticles (aCaPs) lead to enhanced osteoconductivity and enough mechanical properties to withstand the load of the growing tissue during the regeneration process as previously demonstrated [44,45]. Moreover, CaPs have been shown to increase surface roughness, positively influencing the adhesion of ECM proteins to the scaffold, and therefore facilitating cell adhesion and osteoblast differentiation [46,47]. Efficient homogenous distribution of the cells seeded on the porous scaffolds is also essential for an effective scaffold-based bio-regeneration. 3D structures provide the best conditions for cell-cell contact and guarantee a physiological cell environment; however, the penetration capacity of cells seeded on the surface of the scaffold is limited [48]. Mesenchymal stromal cells represent a viable source for developing cell-based therapies for bone regeneration. In particular, human fat tissue has been demonstrated to be a good source of MSCs, the so-called adipose-derived stromal cells (AD-MSCs) [49] Several studies have shown that PLGA/aCaP 3D nanocomposite allows AD-MSCs attachment and proliferation [48,50].

Assessing the integration of the bioengineered scaffold in the native bone at the nanoscale is complex. Among other well-known techniques (micro-CT, histology, electron microscopy), small angle X-ray scattering (SAXS) has become a key method for studying the nanostructure and anisotropy of bone as an arrangement of mineralized collagen fibrils [51–54]. Synchrotron light sources provide significantly higher brilliance compared to laboratory sources, which allows a smaller beam size and shorter exposure. By raster scanning a macroscopic sample and measuring a scattering pattern at each point, the nanostructural heterogeneities of complex structures can be mapped with micrometric spatial resolution. Scanning SAXS has been used as a powerful tool to visualize the nanostructural anisotropy in two-dimensional slices; however, the 2D scattering pattern does not capture the 3D nature of the nanostructure. To complement this method, SAXS tensor tomography (SASTT) [55] uses a combination of 2D projections at different sample orientations, each a full scanning SAXS measurement, to reconstruct the 3D reciprocal space in each voxel, characterizing its local 3D nanostructure. SAXS tensor tomography has been validated [56] and applied to study the orientation of the mineral phase in human bone [57], the healing process around degradable Mg implants [58], and the axon orientation in nervous tissue [59]. A drawback of this technology is the need for synchrotron radiation and the number of required projections for a robust 3D reconstruction that make this method time-consuming.

In this study, we use PLGA/aCaP nanocomposite scaffolds with both randomly oriented and aligned fibers (Scheme 1A), as an alternative for critical-size bone defects regeneration. To obtain a homogeneous cell distribution on the scaffolds, AD-MSCs were first seeded on 2D scaffolds, and osteogenic differentiation was induced. The 2D scaffolds were then rolled along the longitudinal axis creating a 3D structure for *in vivo* testing in a mouse model for critical size bone defects (Scheme 1B). For the aligned scaffolds, the fiber orientation was maintained parallel to the native bone structure. Furthermore, bone regeneration of cell-seeded scaffolds was compared to a decellularized scaffold to investigate whether a bone-mimicking, oriented ECM is sufficient to induce functional tissue formation by harnessing bone's innate regenerative mechanisms. For the analysis, we have employed a combination of 2D scanning SAXS and 3D SAXS tensor tomography to complement more standard methods like histology and micro-CT (Scheme 1C). SAXS tensor tomography provides insight into the 3D arrangement and nanostructure within the critical-sized bone defect 7 weeks after surgery for one sample per group. On the other hand, with 2D scanning SAXS, we cover a larger area, and an increased number of samples could be measured. That allowed us to study, in addition to the quantity of bone formed inside the scaffold, bone quality parameters, such as alignment of collagen, and how the alignment and size of the hydroxyapatite minerals were affected within PLGA scaffolds with random vs directed

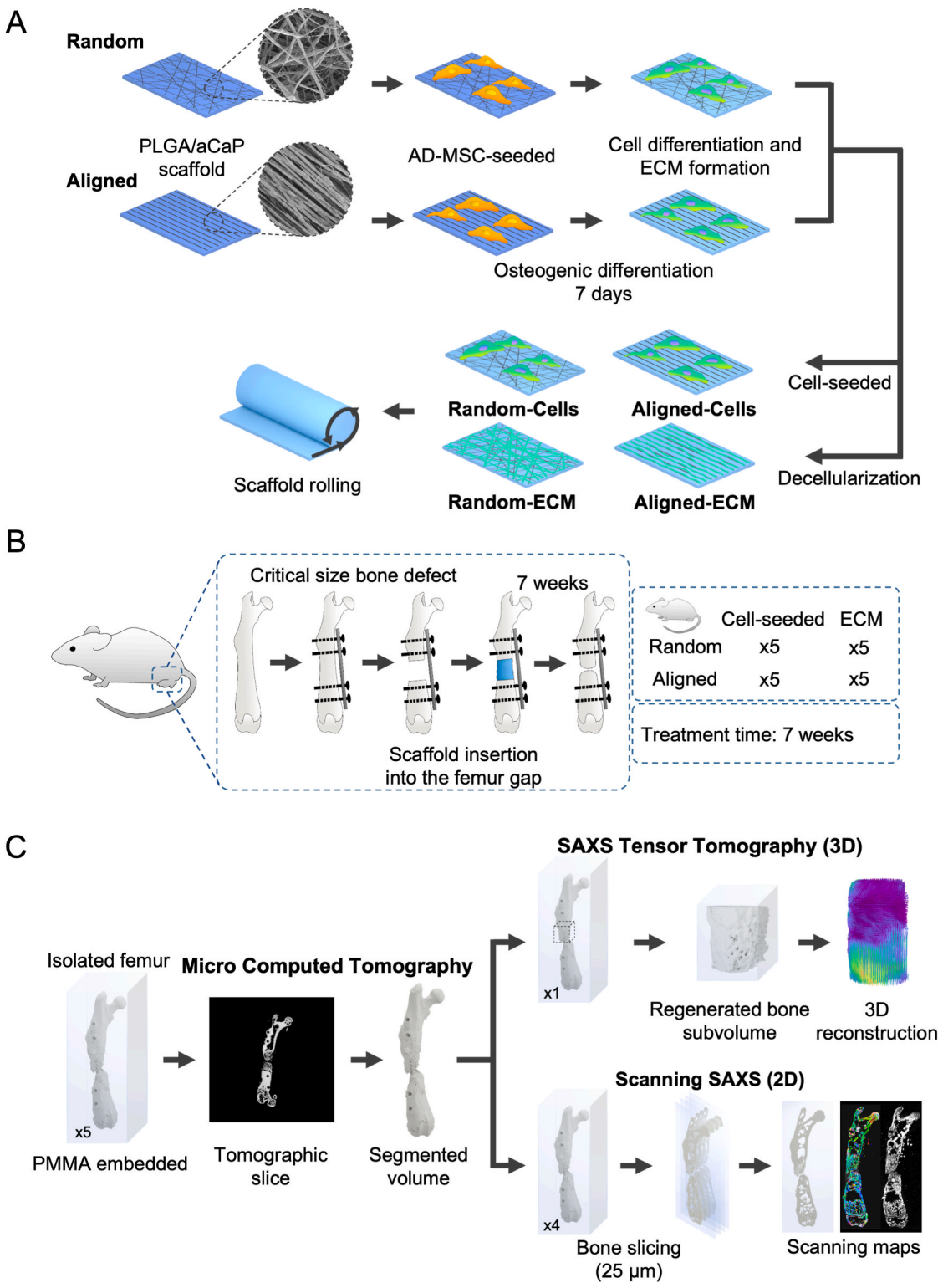

Scheme 1. Experimental procedure. A) Preparation of the scaffold for the *in vivo* experiment. Aligned and random scaffolds were cultured with cells *in vitro* in a 2D shape. That allowed homogeneous distribution of the cells on the entire scaffold area. Before transferring into the mouse's femur gap, cell-seeded or ECM-coated scaffolds were rolled along the longitudinal axis (x-axis), obtaining a 3D structure. Small 3.5 mm thick pieces were cut and immediately transferred into the mouse femur gap. **B)** Workflow of the *in vivo* experiment. Aligned and random scaffolds seeded with AD-MSCs and cultured for 7 days in an osteogenic medium. Half of the scaffolds were, after that, decellularized. In total, four experimental groups were analyzed: Aligned scaffolds seeded with AD-MSCs (n = 5), aligned scaffolds with ECM (n = 5), random scaffolds seeded with AD-MSCs (n = 5), and random scaffolds with ECM (n = 5). Mice were sacrificed after 7 weeks, and bones were isolated for SAXS tensor tomography and micro-CT analyses. **C)** Analysis of isolated femurs after seven weeks. Femurs were embedded in PMMA and analyzed by micro-computed tomography. Afterwards, PMMA blocks were directly used for 3D SAXS tensor tomography measurements or sliced into 25 µm sections to perform 2D scanning SAXS measurements.

alignment as well as scaffolds seeded with AD-MSCs vs ECM after decellularization.

2. Material and methods

2.1. Scaffold material, composition, and sterilization

Clinically approved poly-lactic-*co*-glycolic acid (PLGA; 85% lactic acid: 15% glycolic acid) was received from Boehringer Ingelheim International GmbH, Germany. Amorphous calcium phosphate nanoparticles (aCaP; Ca/P = 1.5) were incorporated produced using flame spray synthesis according to Loher et al. [60] and incorporated into the PLGA in a ratio of 60/40 wt (PLGA/aCaP) according to Ref. [60] Schneider et al. [61] The scaffolds were produced according to Hess et al. [45] (Device: IME EC-CLI, voltage applied: 22 kV to −3 kV, relative humidity: 30%, Temperature: 25 °C, feeding rate: 3 ml/h, distance to collector: 15 cm, tip kept in chloroform air stream: 100 ml/min). The alignment of PLGA-nanofibers was controlled by increasing the speed of the collecting drum (randomly oriented -a.k.a. "random"- scaffold: 200 rpm; aligned scaffold: 2500 rpm). The surface of both aligned and random scaffolds was investigated by scanning electron microscopy (SEM, FEI, Nova NanoSEM 450).

For all experiments, the aligned and random PLGA/aCaP scaffolds were cut into 1 cm^2 squares and placed into 6-well culture plates (Corning). Prior cell seeding, the scaffolds were sterilized in phosphate buffer saline (PBS, Kantonsapotheke Zürich) containing 1.3% 100x amphotericin B (Biowest) and 2% 10 mg/ml gentamicin sulphate (Biowest) for 24 h. Thereafter, the sterilization medium was discarded, and the scaffolds were allowed to air dry in a biosafety laminar flow bench before transferring them into a 24-well culture plate for subsequent cell seeding and culture.

2.2. Tensile properties

The tensile properties of the materials were measured using dumbbells according to Ref. [45]. Briefly, one dumbbell of each material were punched with geometry as given in Fig. 9 aforementioned publication [45]. The mechanical properties were tested using a tensile tester (Shimadzu AGS-X, 100 N load cell, Reinach Switzerland). The gauge length was 15 mm, and the test speed was 1 mm minˆ-1 for both samples. Measurements were made until the failure of the material.

2.3. Origin, culture, and differentiation of adipose-derived mesenchymal stromal cells

All human adipose-derived mesenchymal stromal cells (AD-MSCs) used in this project have been obtained from lipectomies and liposuctions (healthy donors, no diabetic) with the consent of the donors approved by the Ethics Commission of Canton Zurich, Switzerland (KEK-ZH: StV 7–2009), the Swiss ethics (BASEC-Nr.: 2019–01504), and the international ethical guidelines (ClinicalTrials.gov; Identifier: NCT01218945). Generation of AD-MSCs from the stromal vascular fractions (SVFs) was performed according to Zuk et al. [62] and MSC identity was confirmed by following the criteria suggested by the International Society for Cell Therapy (ISCT) [63,64]. AD-MSCs were cultured in Dulbecco modified Eagle's medium (DMEM) (PAN Biotech) supplemented with 10% fetal bovine serum (FBS) (Biowest), 1% of antibiotics (100x penicillin, 100x streptomycin) (Biowest), and 1% L-glutamine 200 mM (Sigma) (called AD-MSC medium). The medium was changed every 3–4 days and cells were passaged with 1x Trypsin-EDTA (Life Technologies) for 5 min at 37 °C when cells were about 80% confluent. The cells were incubated at 37 °C in an atmosphere with 95% humidity and 5% CO_2.

For osteogenic differentiation of AD-MSCs on the scaffolds, sterile scaffolds were seeded with 5×10^5 cells per cm^2. Each 1 cm^2 scaffold was placed into a well of a 24-well plate. 5×10^5 cells were resuspended in 30 μl AD-MSCs medium and distributed dropwise to the upper surface of the scaffold. Cells were allowed to attach to the scaffold for 2 h and thereafter 500 μl of AD-MSC medium was added to each well. 24 h later, the AD-MSC medium was replaced by an osteogenic differentiation medium (Stempro® Osteogenesis Kit; Life Technologies). All cell-seeded scaffolds were incubated at 37 °C, 95% humidity and 5% CO_2. The differentiation medium was replaced every 3–4 days. At the end of the respective culture period, cell-seeded scaffolds were harvested and either fixed in 4% (v/v) formaldehyde (Sigma) for histological analyses or processed for RNA extraction and decellularization procedures, or for the *in vivo* experiment.

2.4. Generation of the extracellular matrix (ECM)

For the generation of the extracellular matrix (ECM), AD-MSCs were allowed to differentiate in osteogenic medium on aligned and random PLGA/aCaP scaffolds. The scaffolds were analyzed after 7 and 14 days of differentiation to assess the ECM deposition. For the decellularization of the scaffolds, three decellularization procedures were tested in order to guarantee the elimination of all cells while fully preserving the structure and functionality of the ECM. All procedures consisted of a chemical treatment followed by a mechanical and finally an enzymatic digestion (Suppl. Figure 2A). Specifically for the chemical treatment, three different detergent solutions were tested: Protocol 1) 0.5% (wt/vol) sodium dodecyl sulphate (SDS; Sigma) in 50 mM Tris-HCL (pH = 8.3); Protocol 2) 3% (vol/vol) Triton X-100 (Roche) in 50 mM Tris-HCL (pH = 8.3); Protocol 3) 4% (wt/vol) sodium deoxycholate (SD; Sigma) in 50 mM Tris-HCL (pH = 8.3). After that, the scaffolds were extensively washed with PBS, and mechanical decellularization was achieved by 12–48 h at −80 °C, followed by thawing at 37 °C for 30min. The scaffolds were then incubated for 12 h in a 500 μl DNase I solution (Qiagen, final concentration 400U/ml) to hamper DNA agglutination. After treatment, the scaffolds were washed with PBS and either fixed in 4% formaldehyde for histological analysis or stored in PBS for cell-seeding or *in vivo* experiments.

2.5. RNA extraction, cDNA generation and quantitative real-time PCR

Gene expression analysis was performed on AD-MSCs differentiated in osteogenic medium on both scaffolds after 3, 7, and 14 days of culture. To this end, RNA was extracted using the RNeasy Mini Kit (Qiagen). Reverse transcription was performed with 250 ng or 500 ng total RNA with oligo-dT primers (Invitrogen), dNTP mix (Invitrogen), DTT (Invitrogen), 5x FS Buffer (Invitrogen), RNA inhibitor (Invitrogen) and SuperScriptIII (Invitrogen). Reverse transcription was carried out with a GeneAMP PCR System (BioRad). Quantitative Real-Time PCR (qRT-PCR) was performed using SYBR Green (Qiagen) and specific primers (Table 1) with a Rotor Gene PCR machine (Qiagen). Cycling conditions were 95 °C for 5 s, 60 °C for 30 s, and 72 °C for 30 s for 40 cycles. Unspecific amplification and primer dimer formation were excluded after analyzing the melting curves. Gene expression was normalized to GAPDH expression and analyzed using the $2^{-\Delta\Delta Ct}$ method [65]. Each sample was measured in triplicates, and all fold changes were calculated relative to the undifferentiated AD-MSCs (day 0 of differentiation).

2.6. Hematoxylin-eosin and Masson Goldner Trichrome staining

AD-MSCs distribution and differentiation, as well as ECM quality after decellularization on both aligned and random scaffolds, were assessed by histochemical analysis. After osteogenic differentiation on the scaffolds, samples were fixed in 4% formaldehyde for 24 h or processed for decellularization as described before and, after that, fixed in 4% formaldehyde for 24 h. After overnight dehydration, all samples were embedded in paraffin.

For Hematoxylin and Eosin (H&E) staining, 3 μm sections were incubated in Mayer's hematoxylin solution (Artechemis) followed by

Table 1
Primer sequences for qRT-PCR.

Gene	Forward Primer	Backward Primer
GAPDH	5′-ACCACAGTCCATGCCATCAC-3′	5′-TCCACCACCCTGTTGCTGTA-3′
CD73	5′-CTCCTCTCAATCATGCCGCT-3′	5′-CCCAGGTAATTGTGCCATTGT-3′
CD90	5′-TGAATACAGACTGCACCTCCC-3′	5′-CTTGACGGGTGAGGCTAGGA-3‘
CD105	5’-TGTCTCACTTCATGCCTCAGCT-3‘	5’-AGGCTGTCCATGTTGAGGAGT-3‘
RUNX2	5’-GAACCCAGAAGGCACAGACA-3‘	5’-GGCTCAGGTAGGAGGGGTAA-3‘
ALP	5’-CCCAAAGGCTTCTTCTTG-3‘	5’-CTGGTAGTTGTTGTGAGCAT-3‘
MSX2	5‘-GCCTCGGTCAAGTCGGAAAA-3‘	5‘-TGACCTGGGTCTCTGTGAGG-3‘
LRP5	5‘-AGGTCGTCGGTGACAGAGTTAC-3‘	5‘-TGTGAAGAAGCACAGGTGGC-3‘
Osteocalcin	5’-CACTCCTCGCCCTATTGGC-3‘	5’-CCCTCCTGCTTGGACACAAAG-3‘

eosin solution (Morphisto). For Masson Goldner Trichrome staining, sections were dipped into Weigert's Iron Hematoxylin solution (Morphisto) for 8 min, followed by Goldner staining solution consisting of Ponceau-acid fuchsin (Carl-Roth) for 15 min. Samples were then washed with 1% acetic acid solution and further stained with Phosphortungstic acid-Orange G (Carl-Roth) for 5 min, rinsed again with 1% acetic acid solution and incubated for 10min in the Goldner staining solution (Carl-Roth). After dehydration and fixation with mounting medium (Pertex), all H&E and Masson Goldner Trichrome sections were stored at room temperature and visualized with a light microscope (Leica, DM6000 B). Hematoxylin stains nuclei in blue-purple, whereas eosin colors proteins non-specifically in pink. Masson Goldner Trichrome stains collagenous tissue in green-light blue and cell nuclei in brown-black color.

2.7. Collagen type I and phalloidin immunostaining

For the visualization of collagen fibers, 3 μm sections were polyclonal antibody (1:100, 30 min RT; Abcam ab34710), followed by 30 min incubation with horseradish peroxidase (HRP)-conjugated secondary anti-rabbit antibody (Dako, K4003). All samples were stained using an automated staining system (Dako CoverStainer). Before antibody incubation, all samples were blocked with a peroxidase-blocking solution (Dako REAL, S2023) for 5 min. For visualization, a substrate-chromogen working solution based on a high-sensitivity DAB (3,3′-diaminobenzidine) system (Dako, K3468) was added to the slides. Samples were counterstained with hematoxylin (Dako), stored at RT and imaged with a light microscope (Leica, DM6000 B). To visualize actin filaments, additional scaffold slides were stained with phalloidin-FITC antibody (1:1000 in PBS, 1% BSA; Abcam ab235137) for 1 h at RT and counterstained with Hoechst dye (1:2000; Sigma Aldrich) for 2 min. Samples were stored at 4 °C and imaged the next day with a light microscope (Leica, DM6000 B).

2.8. Cell viability measurement with AlamarBlue®

To assess the long-term effect of the scaffolds on the cells, the viability of cells cultured on the different scaffolds was measured at various time points over 14 days. 5×10^5 Cells were seeded onto random and aligned scaffolds. AD-MSC medium containing 10% AlamarBlue® (G-Bioscience) was added to each well at 1, 3, 7, 10 and 14 days. Scaffolds without cells served as negative controls. After 3 h of incubation at 37 °C 100 μl of supernatant were transferred in technical triplicates to a 96-well plate. To determine the metabolized dye, the fluorescence was measured at an excitation wavelength of $\lambda_{exc} = 555$ nm and an emission wavelength of $\lambda_{em} = 596$ nm. Afterwards the cells were wash with PBS and cultivated in fresh medium. The measured fluorescence emission was related to the intensity of 100% conversion of the dye.

2.9. Quantitative tissue analysis

The ECM deposited on the scaffolds was compositionally analyzed for hydroxyproline (HYP) as an indicator for collagen, and for glycosaminoglycan (GAG). The scaffolds with cells and decellularized scaffolds were lyophilized, cut in small pieces, and digested at 65 °C for 16 h. The digestion buffer contained 300 μg/ml papain (Sigma-Aldrich) and 5 mM cysteine (Sigma-Aldrich) dissolved in PBS with 5 mM EDTA (Sigma-Aldrich). The amount of GAG in the ECM was determined using a modified method from Farndale et al., [66]. Chondroitin sulphate from shark cartilage (Sigma-Aldrich) was used for a standard curve.

2.9.1. Scanning electron microscopy

Scaffolds with and without AD-MSCs were investigated with scanning electron microscopy (SEM). Samples were fixed with 2.5% glutaraldehyde (Axonlab) and 2% osmium tetroxide (Sigma Aldrich). After dehydration with ascending ethanol gradient solutions (30%, 50%, 70%, 90%, 100%), scaffolds were dried using critical point drying (tousimis). Before SEM analysis, all samples were sputter coated with a 4 nm platinum layer. Images were acquired using scanning electron microscopy (SEM, FEI, Nova NanoSEM 450).

2.10. Scaffold preparation for in vivo experiments

Aligned and random scaffolds were sterilized as described above and cut into 1.5 cm × 2.5 cm rectangles. For the aligned scaffolds, the orientation of the fibers was chosen parallel to the longitudinal axis of the rectangle (Scheme 1A). 2×10^6 AD-MSCs were resuspended in 160 μl AD-MSC medium and distributed dropwise on the scaffolds (final concentration about 5×10^5 cells per cm^2). Cell seeded scaffolds were cultured overnight in 1 ml AD-MSC medium, and the day after, the medium was changed with the osteogenic differentiation medium. All scaffolds were cultured for 7 days under osteogenic differentiation conditions. After that period, half of the scaffolds were decellularized, following protocol 2 mentioned above. The other half of the scaffolds received no treatments and were directly transferred into the mice. On the day of the surgery, scaffolds (2D) were tightly rolled on a very thin injection needle (26G). Rolling was uniform and there was no major variation in the gaps and between the layers of the rolled scaffold. Scaffolds were cut into 3.5 mm long pieces and transferred into the critical size bone defect of the mouse femur.

2.11. Animals, treatment groups and surgical procedure

For this study, twenty 10-weeks old, pathogen-free, and immunocompromised NOD. CB17-prkdscid female mice (Charles River) were used. The animal housing and the study protocol were approved by the Cantonal Veterinary Office, Zurich (ZH 094/2019) and were in accordance with the Swiss Animal Protection Law and the European Directive 2010/63/EU of the European Parliament and of the Council on the Protection of Animals used for Scientific Purposes. Animals were randomly assigned to four treatment groups (5 mice per group): (i) Random scaffold seeded with AD-MSCs, (ii) Random scaffold with ECM (after decellularization), (iii) Aligned scaffold seeded with AD-MSCs, (iv) Aligned scaffold with ECM (after decellularization) (Scheme 1B). Before initiation of each anesthesia procedure, buprenorphine (Temgesic, Reckitt Benckiser) at 0.1 mg/kg animal weight was administered

subcutaneously as a sedative and preventive analgesic. Anesthesia was administrated with a nose mask induced by inhalation of sevoflurane (Sevorane, Abbott) at a concentration of 5–8% in 100% oxygen at a flow rate of 200 ml/min. Surgery was performed according to Manassero et al. [67] The entire surgery was performed under strict aseptic conditions. An osteotomy (critical size bone defect) in the femur was performed by first exposing the anterior surface of the right femur using an anterolateral approach. The skin and the muscle fascia were incised and the M. quadriceps as well as the M. biceps femoris blunt dissected. A drill guide containing the 6-hole Internal Fixator Plate (RISystem, Internal Fixator Plate AO-MouseFix) was aligned with the longitudinal axis on the exposed femur. The plate centered using the flat arms of the drill guide and the pilot holes drilled using a 0.3 mm drill bit. The plate was finally fixated with locking screws (RISystem AG, Davos, Switzerland). The transverse 3.5 mm long mid-diaphyseal femoral osteotomy was then performed using a Gigli saw (0.22 mm; RISystem AG, Davos, Switzerland) with the help of a drill- and saw guide (RISystem AG, Davos, Switzerland), allowing the production of very precise and highly reproducible defects. The resulting critical size bone defect was subsequently filled with an equally sized piece of a scaffold according to the specific treatment groups. The scaffold was fixed in the osteotomy gap with one 2–0 Ethicon Vicryl Plus (Johnson & Johnson international) resorbable suture over the internal fixator plate to prevent displacement of the scaffold from the gap. After scaffold insertion, 5–0 non-absorbable Dermalone sutures were used to close the skin. Analgesic therapy with subcutaneous injection of buprenorphine (0.1 mg/kg) was continued for three days after surgery. After surgery, all animals received adequate care and were monitored for vigilance, pain signs, weight loss and limping three times per day in the first three days, afterwards daily from day 4 to day 7, and finally weekly till the end of the experiment. Seven weeks after surgery, all mice were sacrificed, and femurs were collected for further analysis (Scheme 1B, C).

2.12. Micro-computed tomography

The complete femurs without metallic plate were fixed in formalin and scanned in a micro-computed tomography (micro-CT 40, Scanco Medical AG) operated at an energy of 70 kV and intensity of 114 μA. The scans were executed at a high-resolution mode resulting in a voxel size of 15 μm isotropic. The generated image stack was further segmented into bone, scaffold and background using Avizo 9.4 (ThermoFisher Scientific, Hillsboro, USA). The segmentation of bone was performed by applying a greyscale value threshold to the 3D volume. To measure the amount of regenerated bone in the gap, the center of the closest metallic screw to the scaffold on each side was taken as a reference point, a subvolume was extracted, and the number of voxels corresponding to bone was quantified. In reconstructed images, bone tissue was segmented from background using a global threshold of 12% of maximum grey value. The mean of the volumes of bone within each group was calculated and plotted in GraphPad Prism. One sample from the group aligned-cells and random-ECM was removed from the μ-CT quantification due to damage of the bone surrounding the metallic plate.

2.13. PMMA and bone preparation for small-angle X-ray scattering (SAXS)

All isolated bones were embedded in poly (methyl methacrylate) (PMMA), a transparent synthetic polymer. The formalin-fixed bones were dehydrated using a sequential water substitution process of 24 h in 40% ethanol, 72 h in 70% ethanol (solution replaced every 24 h), 72 h in 96% ethanol and a final dehydration step of 72 h in 100% ethanol (solution replaced every 24 h). Fixation and defatting were performed for 72 h in xylene (solution replaced every 24 h). Plastic infiltration was performed using methyl methacrylate (MMA, Sigma) for one week at 4 °C. Samples were then embedded in MMA containing 0.5% Perkadox 16 S (Dr. Grogg Chemie AG), 15% dibuthylpthalate (Sigma Aldrich), and 0.01% Pentaerythrit-tetrakis-(3,5-di-*tert*-butyl-4-hydroxyhydrocinnamat) (Sigma Aldrich) for 48 h at 4 °C. Polymerization was continued for 24 h at 27 °C. If polymerization did not occur, the temperature was increased for 24–48 h to 37 °C while constantly checking for polymerization progress. Fully polymerized samples were cut using a Mecatome T180 to 25 μm sections (Scheme 1C). All 25 μm sections were fixed on a Kapton tape for the 2D SAXS analysis. One bone-graft specimen from each experimental group was chosen for 3D SAXS analysis. In that case, the PMMA-embedded bone was cut at the extremities to isolate the region of interest around the scaffold (Scheme 1C). A cylindrical sample was shaped by polishing with a metal file.

2.14. Small angle X-ray scattering

Small-angle X-ray scattering (SAXS) experiments were carried out at the cSAXS beamline, Swiss Light Source (SLS) at the Paul Scherrer Institute (PSI, Switzerland) with a micro-focused X-ray beam. A photon energy of 11.2 keV was defined using a Si (111) double crystal monochromator. The beam was vertically focused to 7.5 μm with a bendable mirror. Horizontal focusing was performed by bending the second monochromator crystal, a beam size of 28 μm and 47 μm was used for the 2D measurements and tensor tomography experiments, respectively. An evacuated flight tube was placed between the sample and the detector to reduce air scattering and absorption. The 2D samples were mounted on a motorized stage with movement in 2 axes in the plane perpendicular to the incoming beam (*x*-*y* plane) which allows for raster scan. We conducted the experiments using fly-scanning in the vertical direction (*y*) with a step size of 25 μm and exposure time of 0.035 s. The 3D samples were mounted on a metallic needle in a dual-axis goniometer that allows for rotation, (α) around a tomography axis, which in turn can be tilted around the x-axis (β), and scanning in the *x*-*y* plane [68]. The 3D samples were spatially mapped with a step size of 45 μm and an exposure time of 0.035 s. A total of 211 projections were measured at 6 tilt angles (β) between 0 and 45° and rotation angles (α) between 0 and 180° for a tilt $\beta = 0°$ and 0–360° for $\beta \neq 0°$. The angular step of $\cos(\beta)$ to ensure equal angular sampling for each tilt (angular sampling at $\beta = 0$ was $\Delta\alpha = 5.45°$) [68]. The SAXS patterns at each scanning point were measured with a Pilatus 2 M detector [69] with a sample-to-detector distance of 2.183 m. This configuration covers a q-range from about 0.03 to 5 nm^{-1}, where q is the scattering vector $q = \frac{4\pi}{\lambda}\sin(\theta)$, λ is the X-ray wavelength, and θ the half scattering angle. A 1.5 mm steel beamstop was placed inside the flight tube to block the direct beam to protect the detector. The X-ray fluorescence from the beamstop, which is proportional to the direct beam intensity, was recorded with a CyberStar (Oxford Danfysik) detector and used for transmission correction of the scattering signal [70].

2.15. Scanning SAXS analysis

The scattering patterns for each scanning point were divided in 16 azimuthal segments and integrated using the cSAXS MATLAB package [71]. The scattering signal from the biomineral platelets was analyzed in the range of $q = 0.331$–2.68 nm^{-1} and the "collagen peak" from $q = 0.087$–0.115 nm^{-1}. This collagen peak manifests itself as a multi-order high-intensity peak at 0.095 nm^{-1} (Fig. 4F, red arrow). Its q-values correspond to the collagen fibril D-period, which is enhanced in mineralized tissue due to the presence of minerals in the periodic spacing, This collagen peak signal was extracted from the rest of the signal in each of the 16 azimuthal segments as described for the myelin peak in Georgiadis et al. [59] The anisotropy of the collagen fibrils (using the collagen peak for the latter) was quantified using the procedure described by Bunk et al. [72], fitting a cosine signal to the 16-segment azimuthal intensity. The main direction of orientation was defined by the phase of the cosine and the degree of orientation was calculated dividing the asymmetric intensity by the symmetric intensity.

The mean value and standard deviation of each parameter (e.g. orientation angle, degree of orientation, mineral dimensions, etc.) were calculated for each sample in the region of interest including the callus and gap area (see Fig. 4A and Suppl. Figure 9A). In four samples the uninjured area, i.e. the intact bone, proximal to the induced fracture was quantified and used as a control. The results for each sample group (N = 4) were analyzed using Dunnett's Test for multiple comparisons with control (N = 4).

2.16. SAXS tensor tomography reconstruction

The 2D projections were aligned using an iterative alignment method [73] and the reconstruction of the reciprocal-space map was carried out following a procedure based on that described by Liebi et al. [55,68] The 3D reciprocal space for the mineral platelet in each voxel was reconstructed using a series of spherical harmonics with coefficients a_{ℓ}^{m} with degree $\ell = \{0, 2, 4\}$ and order $m = \{-\ell, -\ell + 1, \ldots \ell - 1, \ell\}$, and the main structure orientation of each voxel determined from the eigenvector associated with the smallest eigenvalue of the rank-2 tensor derived from the reconstructed $\ell = 2$ harmonic [74]. The robustness of the reconstruction was checked by visual comparison of 2D orientation, anisotropy, and degree of orientation between the measurements and simulated projections of the reconstructed data. The degree of orientation was calculated as the ratio between the isotropic tensor coefficient, a_0^0 and the full tensor [68]. The stability of the samples in the X-rays was checked after each full set of rotations at each tilt angle as shown in the radiation damage check in Suppl. Figure 10.

2.17. Mineral particle dimensions

A q-resolved reconstruction was performed in the range q = 0.331–2.68 nm^{-1} on the SAXS tensor tomography datasets in order to extract the mineral platelet thickness. In more detail, the scattering vector q was divided in 180 logarithmically-spaced bins, and a reconstruction of the first coefficient of the spherical harmonics ($\ell = 0, m = 0$) was performed for each of them using as input the azimuthally averaged intensity. The thickness of the mineral particles was calculated assuming platelet shaped particles in a two-phase system with sharp interfaces and a mineral volume fraction of 50%, as described by Fratzl et al. [75,76] The T-parameter was calculated in the range $q = 1.07$–1.66 nm^{-1}, using Equation (1), where P is the Porod constant and J the invariant. The determination of the invariant from the Kratky plot is only possible when the slope of the scattering signal at low q is lower or equal to 2. A power law fitting in the Guinier region of the mineral platelet (q = 0.3–0.9 nm^{-1}) was performed in order to evaluate the slope as described in Liebi et al. [58] The scattering intensity $I(q)$ decays as a function of the amplitude, a, and the exponent, $-G$, as in Equation (2).

$$T = \frac{4J}{\pi P} = \frac{4}{\pi P}\int_0^{\infty} q^2 I(q) dq \qquad \text{Equation 1}$$

$$I(q) = aq^{-G} \qquad \text{Equation 2}$$

3. Results

3.1. In vitro characterization of aligned and randomly oriented electrospun PLGA/aCaP scaffolds seeded with AD-MSCs

To understand whether the orientation of the PLGA/aCaP electrospun fibers influences new bone regeneration *in vivo*, we tested both scaffold types first *in vitro*. Scanning electron microscopy (SEM) images revealed three-dimensional meshes consisting of homogeneous PLGA-fibers with distinct arrangements, aligned or randomly oriented (Fig. 1A), named "aligned" or "random" scaffolds. Contact of the PLGA/aCaP scaffolds with an osteogenic medium containing Ca^{2+} induced the formation of hydroxyapatite crystals, confirming the expected bioactivity (Fig. 1B) and confirming our previous observations [44,77]. We next investigated the viability, distribution, and differentiation of human AD-MSCs cultured *in vitro* on both scaffolds. An essential advantage of using PLGA/aCaP scaffolds instead of cancellous bone pieces is that the synthetic scaffold can also be electrospun with a 2D film shape. A bi-dimensional shape facilitates the homogeneous distribution of the cells on the entire surface of the scaffold, which cannot be reached on the 3D-shaped scaffold due to limited penetration of the migrating cells into the scaffold. Prior to transferring into the femur gap, the cell-seeded PLGA/aCaP scaffolds are rolled up to achieve a 3D shape (Scheme 1A). The scaffolds were designed as bone void filler with limited tensile properties (Suppl. Fig. 11) and are not meant to provide mechanical stability. Immunofluorescence and histochemical analyses of AD-MSCs seeded scaffolds confirmed uniform distribution of the cells over the entire surface ()Fig. 2A. Moreover, cells seeded on the aligned scaffold confirmed the higher degree of orientation compared to the cell-seeded on the random scaffold (Fig. 2A). SEM analyses of both scaffolds cultured in osteogenic medium for 7 days with AD-MSCs demonstrated cell alignment along the fibers (Fig. 1C) but also cell migration from the cell-seeded (upper) side to the bottom side. Cell viability was comparable over the time of culture in both random and aligned scaffolds (Fig. 2F).

We next investigated *in vitro* whether the fiber orientation influences AD-MSCs' osteogenic differentiation potential. To this end, four different AD-MSC lines were cultured for 14 days under osteogenic differentiation conditions on the random and aligned scaffold, and gene expression was investigated after 3, 7, and 14 days. Independent on the fiber orientation, mesenchymal stromal cell markers like CD73, CD90 and CD105 decreased during differentiation (Suppl. Figure 1A). On the other hand, osteogenic markers (early: RUNX2 and alkaline phosphatase ALP; late: Osteocalcin, MSX2, LRP5) rapidly increased their expression confirming the osteogenic commitment of the cells and differentiation towards osteoblasts (Suppl. Figure 1B). Osteogenic differentiation on random and aligned PLGA/aCaP scaffolds was comparable and showed patient-specific variations.

3.2. In vitro generation and characterization of aligned and randomly oriented ECM

The generation of scaffolds possessing an inductive niche would facilitate host cell recruitment and differentiation, leading to an enhanced endogenous regeneration of the tissue. It was demonstrated that scaffolds loaded with an extracellular matrix (ECM) derived from the cultured cells possess a superior biocompatibility than the scaffolds without a pre-deposited ECM [30,78].

We, therefore, examined whether an ECM generated on an aligned scaffold would improve AD-MSCs differentiation *in vitro*. To this end, both scaffold types were cultured with AD-MSCs for 7 and 14 days under osteogenic conditions. During this period, the cells differentiated and generated ECM. Of pivotal importance was then to establish a decellularization protocol, which eliminated all cells while 100% preserving the integrity and functionality of the generated ECM. We tested three different decellularization strategies, which all consisted of a combination of chemical (protocol 1: SDS, protocol 2: TritonX-100, protocol 3: Na-deoxycholate), mechanical (freezing-thawing cycle), and enzymatic treatment (DNase I) (Suppl. Figure 2A). Hoechst staining confirmed the absence of cell nuclei on scaffolds subjected to all three different protocols (Suppl. Fig. 2B and C). Of crucial importance was to determine which protocol best preserved the integrity of the ECM. Investigation of the major abundant fibrous protein present in the ECM, namely collagen I, via a monoclonal antibody and with Masson Goldner Trichrome staining revealed that protocol 2 (chemical treatment with Trion-X-100) was maintaining the best structural integrity of the ECM (Fig. 2B–D, Suppl. Figure 2). SEM images highlighted an intricate network of ECM filaments already after 7 days and confirmed the high efficiency of the optimized decellularization protocol 2 since no structure disruption was

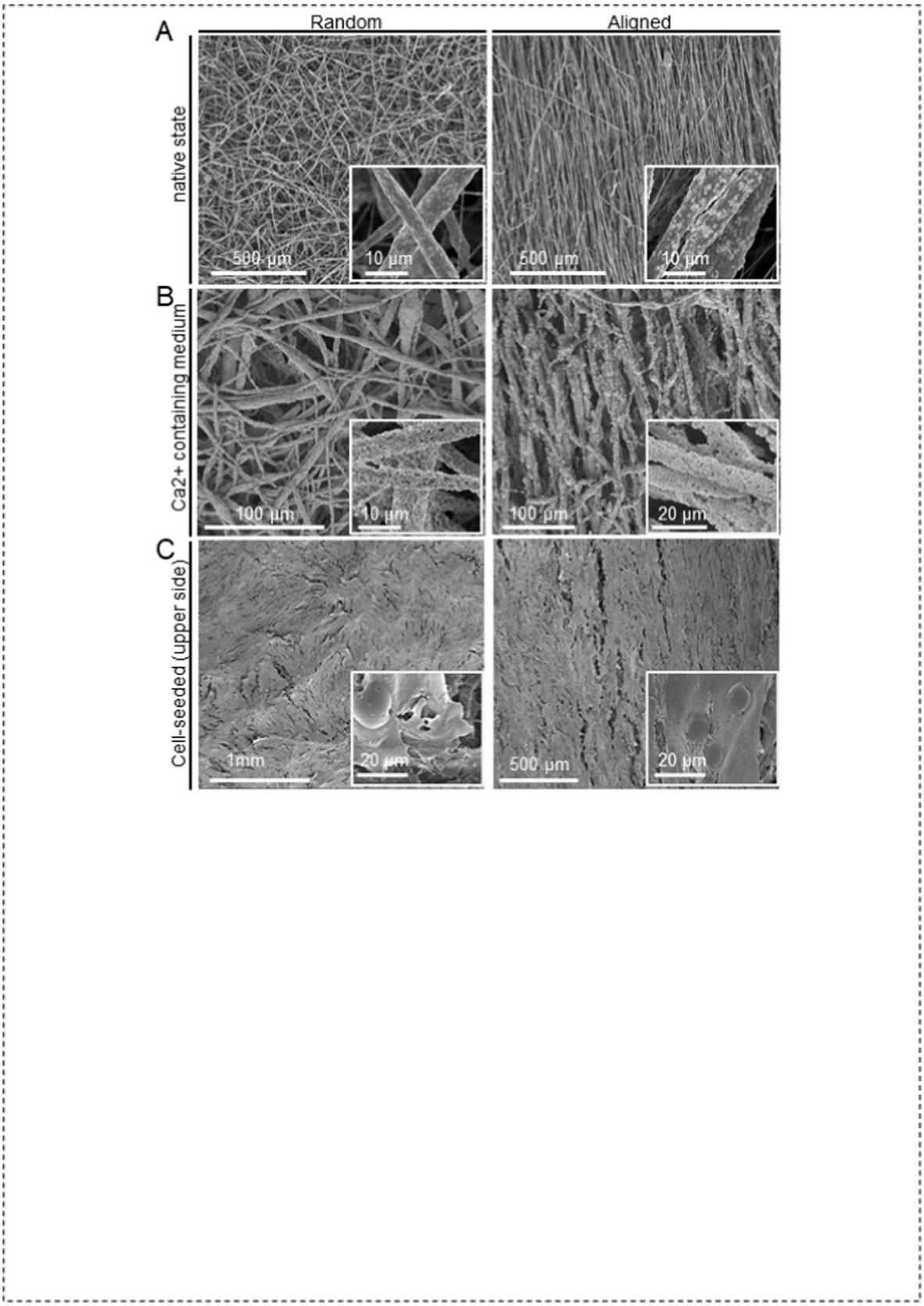

Fig. 1. In vitro characterization of aligned and randomly oriented electrospun PLGA/aCaP scaffolds. A) Scanning electron microscopy (SEM) image overviews of the PLGA/aCaP scaffolds with random (left) or aligned (right) fiber orientation in the native state. **B)** Structure of both aligned and random scaffolds after 7 days of culture in osteogenic medium containing Ca2+, which induced the formation of hydroxyapatite crystals. **C)** SEM images of cell-seeded aligned and random scaffolds confirmed cell alignment along the fibers.

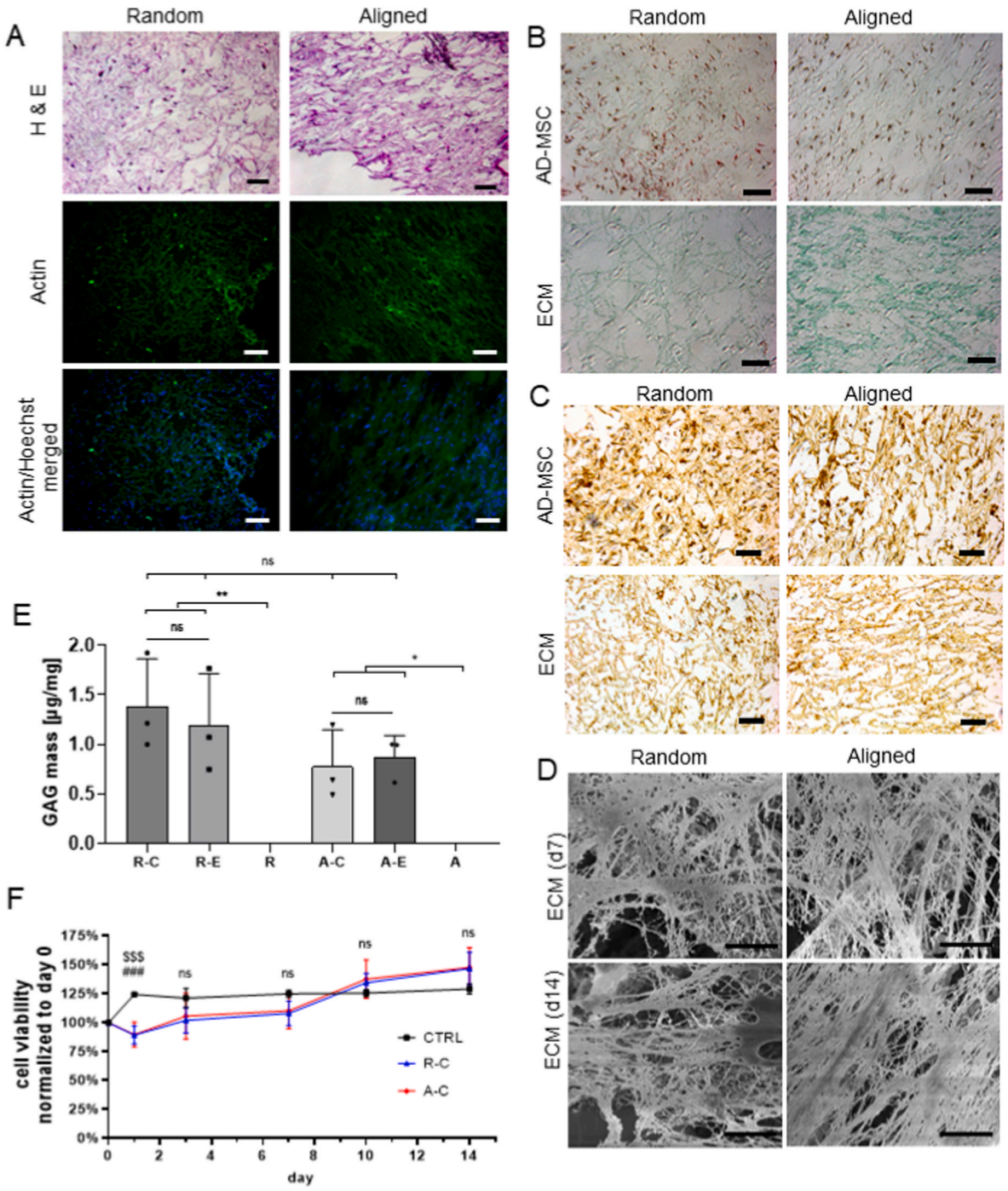

Fig. 2. Characterization of structure of the in vitro generated extracellular matrix (ECM) with protocol 2 (Triton-X-100). A) Hematoxylin and Eosin (H&E) as well as phalloidin-FITC (actin filaments) staining confirmed cell attachment on both scaffolds and cell orientation along the fibers. Cells were counterstained with Hoechst for nuclei visualization. Scale bars 250 μm. **B)** Masson Goldner Trichrome staining of random and aligned scaffold either with cells (control AD-MSC, upper row) or after decellularization with Triton X-100 protocol (protocol 2, Triton-X-100, lower row). Collagen fibers are stained in blue-green, cell nuclei in brown, and cytoplasm in red. An oriented ECM for the aligned scaffold and a randomly oriented one for the random scaffold ECM are visualized. Importantly, the integrity of the ECM was nicely preserved after the decellularization procedure. Scale bar 250 μm. **C)** Visualization of the ECM via Collagen-I antibody staining on cell-seeded (control AD-MSC) aligned and random scaffolds and on decellularized scaffolds. Scale bar 250 μm. **D)** SEM pictures of aligned and random scaffolds decellularized after 7 and 14 days of osteogenic differentiation. Pictures confirmed a well-preserved and abundant ECM after decellularization at both time points. Scale bar 5 μm. **E)** Quantification of GAG on random and aligned scaffolds before and after decellularization. Labels R and A for randomly aligned and aligned scaffolds and C and E respectively for scaffolds containing cells or only extra-cellular matrix. One Way ANOVA followed by Tukey multiple comparison test, *$p < 0.05$, **$p < 0.01$. **F)** To assess the long-term effect of the scaffolds on the cells, the viability of cells cultured on the different scaffolds was measured at various time points over 14 days with an AlamarBlue® assay. CTRl: MSCs cultured on plastic dish; R–C: cells cultured on (Two Way ANOVA followed by Tukey multiple comparison test, $$$ $p < 0.001$ (CTRL vs. R–C), ###$p < 0.001$ (CTRL vs. A-C). (For interpretation of the references to color in this figure legend, the reader is referred to the Web version of this article.)

observed (Fig. 2D). In order to quantify the composition of ECM present on random and aligned scaffolds before and after decellularization the amount of glycosaminoglycans (GAG) was quantified. No significant differences could be detected between random and aligned scaffolds (Fig. 2E).

To assess the ECM functionality and exclude potential cytotoxic effects of the chemical compounds used for the decellularization protocols, we tested *in vitro* AD-MSCs viability cultured on aligned and random PLGA/aCaP scaffolds with pre-deposited ECM. Initially, aligned and random scaffolds were seeded with AD-MSCs and cultured under osteogenic conditions for 7 days to generate ECM. After that, the three decellularization protocols were applied, and the scaffolds were re-seeded with undifferentiated AD-MSCs. The re-seeded scaffolds were then cultured for 14 days, and gene expression was investigated after 3, 7, and 14 days. Generally, the MSC markers CD73 and CD90 decreased in all samples, while the early osteogenic markers ALP and RUNX2 increased during differentiation (Suppl. Fig. 3A–C). These data confirmed that none of the decellularization protocols used had adverse effects on RNA expression levels, an indication of cell viability and healthy differentiation. Since collagen I fibers were better maintained by using TritonX-100, all decellularization procedures were then performed by following that protocol.

3.3. Regeneration potential of aligned and random PLGA/aCaP scaffolds in a mouse model for critical-size bone defect

The regenerative potential of aligned versus random PLGA/aCaP scaffolds seeded with AD-MSCs or coated with AD-MSC-derived ECM was investigated *in vivo* in a mouse model for femoral segmental critical-size defect. In this model, stabilization of the large bone defect was obtained through an internal fixation with a titanium micro-locking plate as described in Manassero et al. [67] A 3.5 mm long segmental bone defect was induced in the mid-shaft of the femur. Cell-seeded or decellularized scaffolds with aligned and randomly oriented PLGA fibers were implanted into the bone gaps. AD-MSC-seeded aligned and random scaffolds were cultured *in vitro* for 7 days in an osteogenic medium. On the day of the surgery (day 7 of the culture), the cell-seeded scaffolds were rolled, cut into 3.5 mm long pieces, and immediately transferred into the femur gap. Aligned and random decellularized scaffolds were prepared in advance and stored at −80 °C until surgery. Importantly, scaffolds were rolled along the longitudinal axis (Scheme 1A). In this way, the PLGA fibers of the aligned scaffolds were parallel to the native bone main fiber orientation. In total, four treatment groups were investigated: i) Aligned scaffold with AD-MSCs, ii) Aligned scaffold with ECM, iii) Random scaffold with AD-MSCs, iv) Random scaffold with ECM (Scheme 1 1 A). MicroCT analysis of the isolated femurs 7 weeks post-surgery, revealed mineralization within all treatment groups (Fig. 3A and Suppl. Fig. 4A–D). Total bone volume analysis of the newly formed bone tissue in the critical size gap revealed no significant differences regarding the amount of new bone formed between the different groups (Fig. 3B). However, aligned scaffolds with either AD-MSCs or ECM showed a trend toward increased bone formation compared to random scaffolds. A striking difference was nevertheless visible at a structural level. Whereas in the aligned scaffold, osseointegration of the scaffold was visible and new bone formation was occurring, in the random scaffold, new bone formation was somewhat uncoordinated and generated disconnected islands of bone reminiscent of pseudo-arthrosis (Fig. 3A and Suppl. Fig. 4A–D). Osseointegration failure was observable in all random scaffolds independently if seeded with AD-MSCs or with ECM only (Fig. 3 and Suppl. Figure 4). The superiority of aligned scaffold over random scaffold was also highlighted by the observation that in some of the samples, the gap was almost completely closed through newly formed bone.

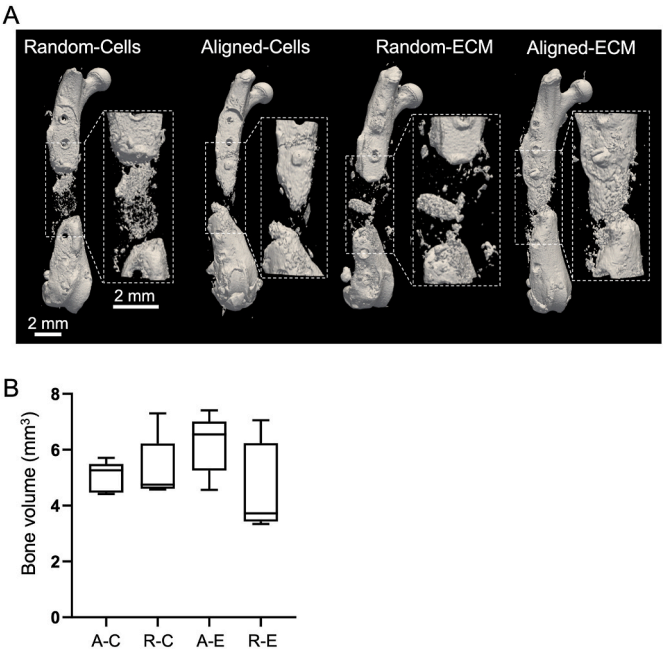

Fig. 3. Quantification of bone regeneration in the in vivo mouse model for critical size bone defect. A) Isosurface rendering of the three-dimensional reconstruction of microcomputed tomography images of one representative femur for each experimental group isolated after 7 weeks. Marked with dashed lines is the region of interest where the gap was originally generated. **B)** Quantification of the new bone regeneration, labelled R and A for the randomly aligned and aligned scaffolds respectively and containing cells C or only extracellular matrix ECM. The box plot shows the minimum and maximum, the median (50% percentile) and the 25% and 75% percentiles. The amount of bone in the gap was quantified by accounting for the number of voxels in a subvolume defined using the same reference points for each bone. Random scaffold with cells (n = 5), aligned scaffold with cells (n = 5), random scaffold with extracellular matrix, ECM, (n = 4) and aligned scaffold with ECM (n = 5).

3.4. Influence of the scaffold structure on the bone nanostructure

The influence of the morphology of the scaffold on the nanostructure of the regenerated bone was assessed using SAXS. With this technique, it is possible to study the anisotropy of the organization of the biomineral phase, i.e. hydroxyapatite nanoplatelets and collagen fibrils. In order to get a macroscopic overview of the bone anisotropy, the femurs were sliced and measured using scanning SAXS, Fig. 4. The scattering signal of bone in a representative scanning point is shown in Fig. 4F, and its azimuthal integration in Fig. 4G, where the respectively analyzed *q*-ranges for the scattering of the mineral platelets and the collagen peak are shown. The direction and degree of orientation were extracted for the mineral platelets (Fig. 4A and B and Suppl. Figure 8) and collagen fibrils (Suppl. Figure 5A-6B and Suppl. Figure 9). In the aligned scaffolds, the overall orientation of the bone nanostructure showed mineral platelets and collagen fibrils ordered along the femur long-axis. On the other side, scaffolds with randomly aligned fibers showed a rounded callus with orientation perpendicular to the femur long-axis and a low degree of orientation. That was also clearly visible in the dot product between the direction of orientation and the femur long-axis (Suppl. Figure 4C and Suppl. Figure 6A), with a value close to 0 when the orientation is perpendicular to the bone direction and close to 1 when it is parallel. The aligned scaffolds in Fig. 4 and Suppl. Figure 8 showed a higher amount of bone in the callus area, with an orientation parallel to the bone direction (dot product of SAXS-derived microscopic fibril orientation with bone direction close to 1, Suppl. Figure 5C and Suppl. Figure 6A), similar compared to the direction of orientation in the native bone indicating a high degree of osseointegration. The aligned scaffold with ECM contains a higher amount of new bone with a higher dot

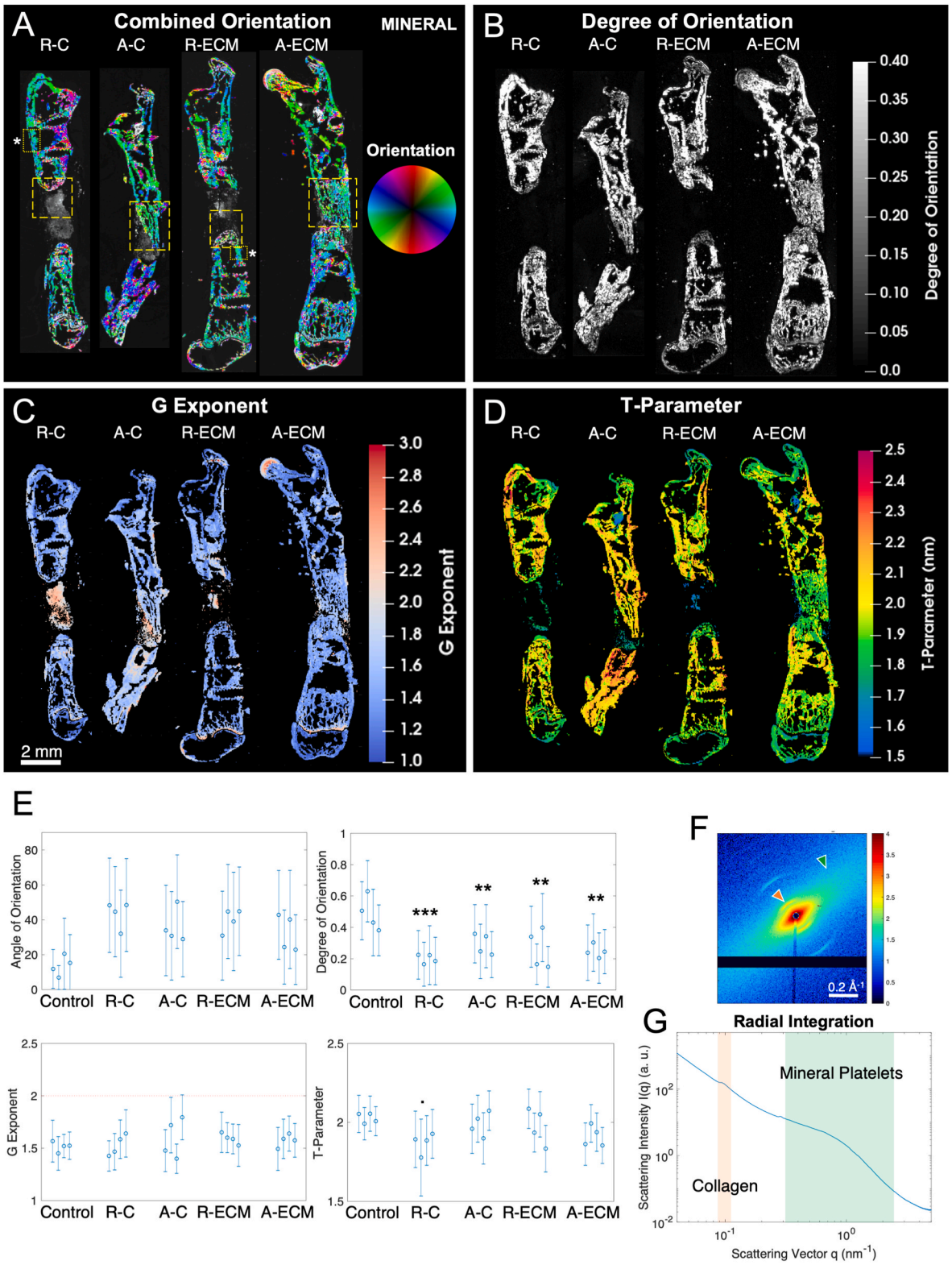

(caption on next page)

Fig. 4. Anisotropy of the bone nanostructure visualized by scanning SAXS. Scanning SAXS of bone sections with scaffolds with random and aligned fibers, labelled R and A, respectively, and containing cells C or only extra-cellular matrix ECM. **A)** The orientation and scattering intensity are color-coded according to the color wheel, where the hue shows the direction, and the value shows the symmetric intensity. Additionally, the saturation shows the asymmetric intensity [72]. Highly oriented material appears with bright colors whereas low-oriented material appears in grayscale, with the grey value proportional to the total scattering intensity. **B)** Degree of orientation of the scattering signal from the q-range corresponding to the mineral platelets (q = 0.331–2.68 nm-1). Of note, the orientation of minerals is perpendicular to that shown by the color wheel since scattering occurs perpendicular to the mineral main direction. This is the opposite of what happens in the case of the collagen fiber peak, for which scattering is strongest along the fiber direction (Suppl. Fig. 7A) **C)** The G exponent of the mineral platelets at low q (Equation (2)) and **D)** the T-parameter, which represents the mineral particle thickness in nm, are shown according to the color scale. **E)** Quantification of the direction of orientation, degree of orientation, G exponent, and mineral thickness in the callus and gap area of each sample group (region of interest highlighted in dashed lines in A and Suppl.)Fig. 10A. The region of interest of the area used as a control is shown in dotted lines with a star symbol in A and Suppl. Fig. 10A. Each distribution represents all points within a bone (4 specimens per group). Dunnett's multiple comparison test was used to compare the control values of not damaged bone with the different scaffolds. · $p < 0.1$, *$p < 0.05$, **$p < 0.01$, ***$p < 0.001$. **F)** A representative inset of a scattering pattern from one scanning point in the bone area, showing 210 × 240 pixels of the 1475 × 1679 total number of pixels on the detector. The black horizontal line is due to a gap between the detector modules. **G)** Azimuthal integration for the pattern in (F), in which the signal of the first order diffraction of the collagen peak (red triangle in F) and the q-values where the scattering signal of the mineral platelets was evaluated are highlighted (green triangle in F). (For interpretation of the references to color in this figure legend, the reader is referred to the Web version of this article.)

product, which is a sign of more advanced growth. These results indicate a correlation between the scaffold type and the degree of orientation at these length scales. On the other hand, poorly aligned tissue with a low degree of orientation was observed in the gap of both random scaffold groups, visualized with grey color in the gap of the random bones (Fig. 4A–D, Suppl. Figure 8 and Suppl. Figure 9) and in the symmetric intensity (Suppl. Figure 5D and Suppl. Figure 6B). As already seen in the micro-CT analysis, this tissue is isolated from the rest of the bone, and it cannot be associated with a growth process from the bone towards the gap. In that region, a G exponent higher than 2 is observed (Fig. 4C). High G exponent has been associated with areas where the bone is being formed, and where the mineral nanoparticles have a more rounded shape than the typical platelet-like shape [79]. The combination of non-defined orientation, low degree of orientation and high G exponent could indicate the presence of tissue with certain mineral content but without the characteristic nanostructure of bone, such as ordered collagen fibrils mineralized with platelet-like particles. The T-parameter cannot be calculated since the platelet-like assumption is not fulfilled (Fig. 4D). These data further corroborate the observation that random scaffolds lack osseointegration. We further aimed to determine the mineral platelet thickness by using the T-parameter for points in which the G exponent was equal to or lower than 2 (Fig. 4C). A mineral thickness of 2.03 ± 0.06 nm is observed in the bone area [80] and lower values between 1.87 ± 0.04 and 1.98 ± 0.07 nm for the random and aligned scaffolds in the callus (Fig. 4D).

For further statistical analysis, the region of interest containing the callus and gap was individually analyzed for each bone. The mean value and standard deviation of the pixels in those areas were combined for each sample group, and the sum of their values was plotted in Fig. 4E. A multiple comparison statistical analysis was performed using the Dunnett's Test with the healthy bone away from the implant side as a control. The mean values of the degree of orientation present significant statistical differences, with the random scaffold with AD-MSCs being the one with the lowest mean values, indicating random platelet orientation. A similar trend can be observed in the orientation of the mineral platelets calculated as the dot product with the femur long-axis in Suppl. Figure 6C.

To better understand the nanostructure in the 3D volume of the scaffold, a small volume containing part of the native and regenerated bone in one femur per animal group was measured using SAXS tensor tomography. The measured volume corresponding to its respective femur is shown in dotted lines in the 3D reconstruction of the micro-CT data in Suppl. Figure 4. The *q*-resolved reciprocal-space map on a range relevant to the mineral platelets was reconstructed in each voxel of the 3D volume, as described in the methods section, and the visualization of the anisotropy is plotted in Fig. 5A and visualized in the 3D render in Suppl. Video 1-4. The direction of the mineralized collagen fibers is represented by the direction of the cylinders and the degree of orientation by the color scale. There was a clear visual difference between the amount of regenerated bone in the random and aligned scaffolds independent of the presence of AD-MSCs or ECM (Fig. 5). Scaffolds with random fibers showed poor growth in the gap and a rounded morphology in the callus. The aligned scaffold presented a more advanced growth with a cylindrical shape, which filled almost all the available space in the gap (Fig. 5). This is also clearly visualized when the three-dimensional dot product between the voxel orientation and the bone long-axis is calculated (Suppl. Figure 7D). A wider distribution of values, with dot products reaching values below 0.5 are found in the callus of random scaffolds with cells and with ECM, which indicate orientation perpendicular to the bone axis, while orientations parallel to the bone axis give values close to 1 in both aligned scaffolds groups (Suppl. Fig. 7A-C). Representative 2D slices of the 3D volumes are shown in Fig. 5C. As for the 3D volume, in the random scaffolds, also the orientation of the nanostructure in the callus presented a rounded shape, which followed the rounded surface closing the edge of the cut and not showing any advanced growth into the gap. In contrast, the nanostructure of the callus in the aligned scaffolds followed the direction of the long axis of the femur and had similar morphology to the original bone (Fig. 5C), which is an indicator of an advanced regeneration process. That indicated a correlation between the orientation of the scaffold fibers and the nanostructure of the regenerated bone. A general lower degree of orientation was observed in the regenerated area than in the native bone, independently of whether they contained AD-MSCs or only ECM (Fig. 5E). Additionally, the *q*-resolved reconstruction allowed to calculate the T-parameter, which is shown in the 3D isosurface renderings in Fig. 5B and representative 2D virtual slices in Fig. 5D. The values of the mineral thickness, calculated as the mean T-parameter, for the native bone is 2.18 ± 0.19 nm, as expected [80]. The regenerated bone in the callus of the random scaffolds shows a mean T-parameter of 2.04 ± 0.13 nm, while the aligned scaffold with ECM has a mean T-parameter of 2.14 ± 0.11 nm (Fig. 5F).

4. Discussion

Repairing large bone defects is a surgical challenge. These defects are currently treated by either using autologous bone tissue, allogeneic and xenogeneic demineralized bone matrix, or synthetic graft materials such as ceramics, metals, or polymers [30,81–83]. However, these approaches harbor several drawbacks associated with donor site morbidity with autologous bone tissue, the potential for disease transmission with allogeneic and xenogeneic tissue and lack of biodegradability for most metals and some ceramics [11,83,84]. These limitations could be overcome by using tissue-engineered grafts composed of biocompatible and biodegradable scaffold materials combined with an osteogenic cell source to support the body's intrinsic capacity to regenerate bone. One of the requirements for scaffolds used for bone tissue engineering is to mimic the structure and function of native bone ECM to promote host cell migration into the scaffold and promote osseointegration, thereby

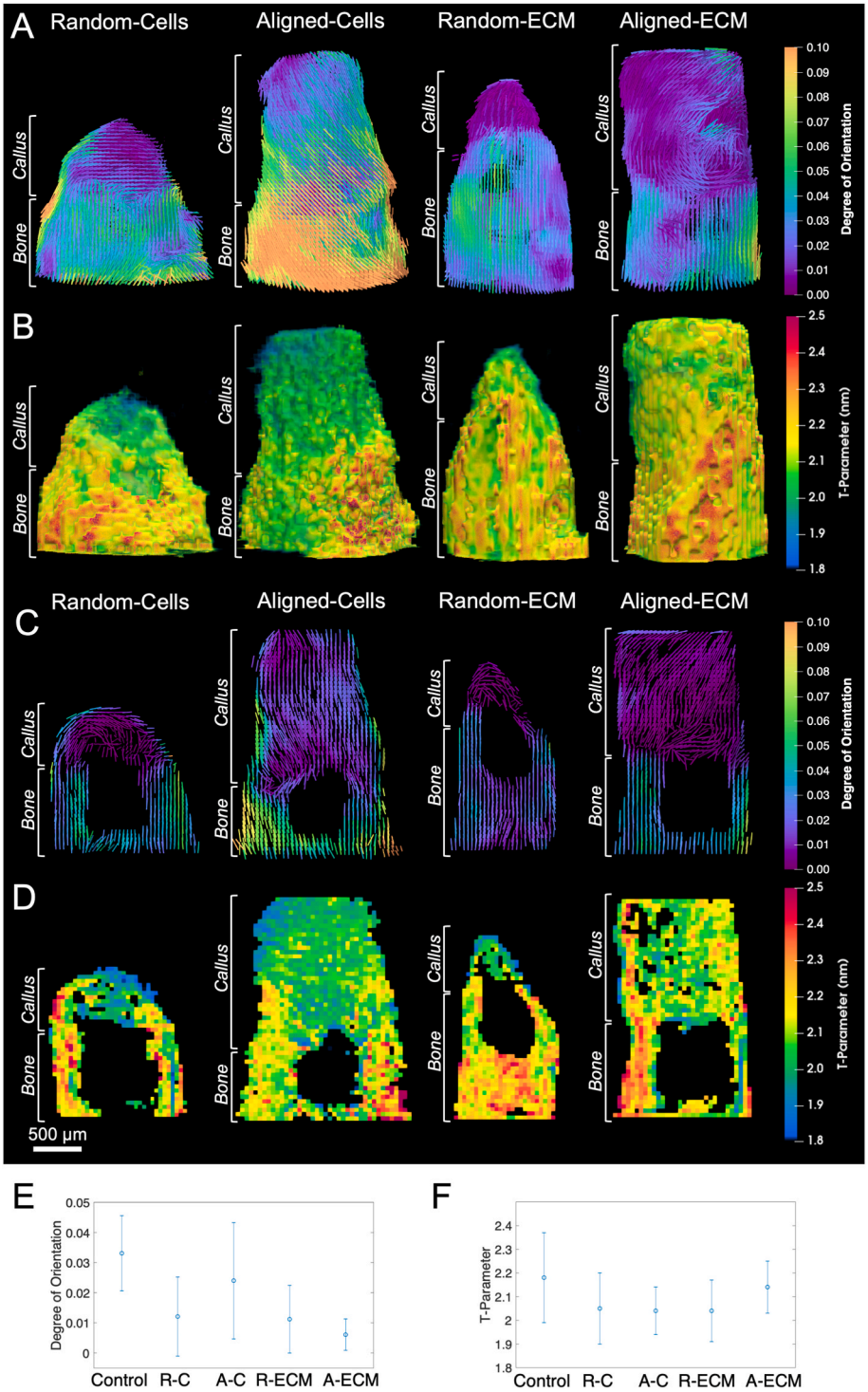

Fig. 5. SASTT reconstruction of the orientation of the scattering of the mineral platelets in the regenerated bone. A) 3D representation of the direction of anisotropy of the spatially resolved scattering signal corresponding to the mineral phase and **B)** thickness of the mineral particles, **C, D)** Representative 2D virtual slice of each sample taken from the middle position. The direction of the cylinders shows the direction of orientation and the color scale the degree of orientation. The T-parameter, which represents the thickness of the mineral platelets in nm, is plotted in the 3D volume and the 2D slice according to the color map. **E, F)** Quantification of the degree of orientation and T-parameter for each tomogram in the callus. The undamaged native bone in the femur with aligned-ECM was used as a control. (For interpretation of the references to color in this figure legend, the reader is referred to the Web version of this article.)

enhancing new bone formation. Mimicking the native structure of bone ECM with its highly hierarchical organization at the nanometer scale is nevertheless complicated and one of the main challenges in bone tissue engineering [85].

In the present study, we have postulated that using aligned PLGA/aCaP nanocomposites with AD-MSCs or their ECM could be a promising bone tissue engineering approach that would result in a better organized and faster bone regeneration process. Previous works by others and we have shown that PLGA/aCaP scaffolds provide the advantages of a biocompatible and degradable polymer and a mineral component, allowing us to optimize the physical and biological properties required for a scaffold material aimed at bone reconstruction [48,50,86–89]. The nanocomposite scaffolds we used in this study mimic not only the structure but also the organic and inorganic composition of native bone ECM, even though is not supposed to provide mechanical stability, which is provided through the plates. This is also confirmed by the limited tensile properties of the material (Suppl. Fig. 11) which highlight the applicability as bone void filler. The organic part with its highly organized collagen fibers is mimicked by the aligned PLGA nanofibers, whereas the amorphous CaPs mimic the inorganic component of native bone ECM. The alignment of PLGA-nanofibers was controlled by increasing the speed of the collecting electrospinning drum in order to

generate both random and aligned mashes. The AD-MSCs employed for this work were previously characterized for their cellular identity and differentiation capacity [64,90]. *In vitro* testing of the scaffolds indicated that the cultivation and differentiation of AD-MSCs on both types of scaffolds were similar. Thus, fiber orientation did not directly influence the differentiation ability of the cells. That was expected because both scaffolds were generated with the same material, and thus the fibers possessed the same nanoscale topography.

We previously observed that the migration capacity of cells into the scaffold upon seeding is limited [48]. To ensure homogeneous distribution of the cells all over the scaffold, we produced 2D scaffolds rolled shortly before implantation to obtain the needed 3D diameter to fill the gap. With this approach, cells are cultured on the 2D scaffold *in vitro*, ensuring a better exchange of nutrients, metabolic waste and oxygen. Moreover, a homogeneous distribution of the cells on the entire scaffold surface is ensured and on the inside of the graft. SEM analysis confirmed that the alignment and orientation of the cells along the PLGA-fibers were uniform throughout the entire scaffold, confirming that the cells attached to the scaffold's nanofibers could migrate to the opposite side of the scaffold. Scaffold architecture resulted in a higher degree of orientation and alignment of cells seeded on an aligned scaffold compared to the random. Moreover, SEM analysis together with immunohistochemical collagen-I staining highlighted the formation of an oriented ECM on aligned scaffolds. In comparison, an ECM deposited on a random scaffold showed a lower degree of orientation and alignment.

Calcium is a key player in several signaling pathways [91,92] and changes in free calcium ion concentration can lead to non-physiological changes, which might be harmful to the cells. In contrast to the *in vivo* situation where the calcium concentration is maintained constant as Ca^{2+} is continuously delivered to sites with transiently lowered concentrations, *in vitro* enhanced Ca^{2+} deposition, as observed for highly osteoconductive materials, may lead to Ca^{2+} depletion from the media and potentially affect the commitment of MSCs [44,93]. Our SEM data clearly indicated the presence upon cultivation of an increased surface roughness of the nanofibers due to the incorporated aCaP-nanoparticles. Furthermore, SEM pictures revealed the formation of a continuous layer of hydroxyapatite crystals on the surface of the fibers confirming that the aCaP serves as a precursor of hydroxyapatite crystal formation. Of interest, differential-shaped osteoblasts could be observed, ranging from flat to plump, thereby reflecting their level of cellular activity. Increased surface roughness through aCaP affects protein adhesion leading to cell adhesion [46]. These characteristics are fundamental because scaffold surface and porosity are peculiar requirements for *in vivo* bone ingrowth and vascularization. As expected, cells seeded on the aligned PLGA/aCaP nanocomposites showed preferred orientation along the fibers and production of aligned collagen fibers/ECM following the principle of contact guidance [40]. Interestingly, SEM images already revealed an extensive ECM formation after 7 days of osteogenic differentiation for both types of scaffolds.

In the past years, the use of decellularized ECM alone or in combination with other biologics has gained importance in the fields of regenerative medicine and tissue engineering. Decellularized ECM can recapitulate native tissue and can be employed to increase the biochemical, mechanical, and vascular milieu of damaged tissues. Furthermore, naturally derived biomaterials have proven to be superior to synthetic polymers in that they can retain the hierarchical complexity of native tissues [94,95]. We have hypothesized that incorporating a decellularized ECM in the porous synthetic PLGA/aCaP scaffold would create an environment that better mimics the structure and the function of native bone ECM, particularly in the aligned scaffold setup. We, therefore, developed a decellularization strategy that removed cells and genetic material efficiently while preserving the structural and functional integrity of the ECM by limiting the damage to the scaffold material. As implantation of incompletely decellularized scaffolds can evoke host foreign body reactions, we first tested the efficacy of different decellularization protocols. The combination of 3% TritonX-100, DnaseI digestion and freezing delivered the best results: Lack of cells and visible nuclear material, the integrity of the collagen fibers, preservation of the scaffold fiber alignment and degree of orientation. In contrast to scaffolds with cells which need immediate transfer to the host, decellularized scaffolds have the advantage that they can be stored for a longer time at −80 °C.

Even though *in vitro* evaluation of bioengineered scaffolds reveals important information on cytocompatibility and osteogenicity, only *in vivo* implantation can deliver sufficient information on their performance in the desired environment. We, therefore, performed the orthotopic implantation of the scaffolds in a mouse model for critical-size defects [67]. This model provides information regarding the integration of the construct with surrounding tissue and how well it sustains the union of an otherwise non-healing bone defec [96].

Analysis of the femurs was performed seven weeks post-surgery to monitor the healing process before complete gap closure occurs. Interestingly, we could not assess any statistically significant difference regarding the total amount of newly formed bone tissue within all treatment groups. Nevertheless, there was a striking difference in the quality of the newly produced bone and the osseointegration properties of aligned versus random scaffolds. The aligned scaffold showed a high degree of osseointegration and promoted new bone formation with the same orientation as the native bone. That was also mirrored in the nanostructure of the newly formed bone, showing mineral platelets and collagen fibrils ordered along the femur long-axis. Furthermore, the aligned scaffold presented a more advanced growth with a cylindrical shape, which filled almost all the available space in the gap. In contrast, scaffolds with random fibers showed a rounded callus with orientation perpendicular to the femur long axis, and new bone formation generated disconnected islands of poorly aligned tissue, reminiscent of pseudoarthrosis. This observation was corroborated by the nanostructure SAXS measurements that clearly showed a combination of non-defined orientation, low degree of orientation and high G exponent in random scaffolds, indicating the presence of tissue with certain mineral content but without the characteristic nanostructure of bone such as ordered collagen fibrils mineralized with platelet-like particles [79]. The superiority of aligned scaffold over random scaffold was also highlighted by the observation that in some of the samples, the gap was almost completely closed through newly formed bone. Those areas were found to have a higher mineral thickness, which is representative of an ongoing regeneration process [97].

The performance of aligned decellularized scaffolds was very similar to that of aligned scaffolds seeded with cells. Both scaffolds generated new bone with similar morphology to the original native bone. Aligned scaffolds with ECM had a visible porosity in the callus area and a more homogeneous volume shape than the aligned scaffold with cells. In addition, a higher mineral thickness, i.e. T-parameter, indicates a more advanced regeneration process, as found in other studies [97] where more mature mineralized tissue in the callus was composed of thicker mineral particles (higher T-parameter). This observation is very interesting because it suggests that an appropriate amount and orientation of ECM are sufficient to promote bone regeneration and migration of endogenous cells from the native bone into the scaffold.

In the results presented in this study, histology and micro-CT are combined with X-ray scattering imaging techniques. Histology is a convenient and well-established method to study the morphology of thin slices of biological tissue. In computed tomography, a 3D reconstruction of the sample can be created based on its X-rays absorption or density. Both methods offer interesting opportunities for biology, but they lack crucial information about the morphology and arrangement of collagen and biominerals, their specific crystalline or amorphous phase and particle shape/size. Scattering imaging techniques can provide structural information on the precise arrangement of nanostructures at a microscopic level. Scanning SAXS and SAXS tensor tomography adds a new dimension to this study, visualizing the sample's shape and

components' spatial distribution and accessing valuable information about the specific nanostructural arrangement and their anisotropy. Even though high-intensity focused X-ray beams are necessary, which only a synchrotron can provide, the information obtained using scanning SAXS and SAXS tensor tomography is very valuable when assessing the quality of newly formed bone.

5. Conclusion

Our data indicate that aligned PLGA/aCaP nanocomposites seeded with AD-MSCs or loaded with AD-MSCs-generated ECM are superior to random PLGA/aCaP scaffolds. Even though both types of scaffolds possess similar cytocompatibility and osteogenicity *in vitro*, they show *in vivo* significant differences in osseointegration and bone regeneration capacity. These differences were particularly clear through 2D scanning SAXS and SAXS tensor tomography, which allows to analyze of three-dimensional bone nanostructure and offers the unique chance to correlate spatial nanoscale features at relatively long distances. At present, fabricated implants typically suffer from poor osseointegration and tissue formation. The similar properties observed *in vivo* between aligned scaffolds containing either cells or only ECM highlights the possible advantage of using only the ECM for the preparation of bio-engineered bone scaffolds. Decellularized matrices as scaffolds have the advantage of mimicking the tissue to be replaced and triggering scaffold repopulation with the patient's cells. Therefore, using ECM would be particularly interesting in preparing out-of-the-shelf grafts for bone regeneration. Decellularization of the ECM with autologous cells could help prevent host rejection and fibrosis and eliminate the need for long-term immunosuppression.

Author contribution

EAC performed *in vitro* and *in vivo* experiments, prepared samples for *ex vivo* analyses and wrote the manuscript, ARP prepared the samples, performed the synchrotron experiments, performed data analysis for the scattering and μ-CT experiments, and wrote the manuscript, LS performed *in vitro* experiments, KA performed GAG and cell viability analysis, MG performed GAG analysis, OG generated the scaffold and performed SEM pictures, YN performed μ-CT measurements, and manuscript editing, ST performed surgical procedure, APD prepared PMMA samples, MGS performed the synchrotron experiments and q-resolved analysis, ZG performed the synchrotron experiments, CA performed the synchrotron experiments, LN wrote the SASTT reconstruction algorithm, MG developed the collagen peak extraction algorithm, FEW supervised the preparation of PMMA samples and edited the manuscript, HCP supervised the study, edited the manuscript, WS supervised scaffold production, edited the manuscript, PC conceived and supervised the study, performed *in vivo* experiments, assisted in data analysis, and wrote the manuscript, ML conceived and supervised the study, performed the synchrotron experiments, assisted in the data analysis, and wrote the manuscript.

Declaration of competing interest

The authors declare that they have no known competing financial interests or personal relationships that could have appeared to influence the work reported in this paper.

Data availability

Data will be made available on request.

Acknowledgment

Ines Kleiber-Schaaf and Andrea Garcete-Bärtschi for the preparation of the bone slides for histology analysis. Debora Wanner for support with the GAG analysis. This work has been supported by the Area of Advance Material Science at Chalmers University of Technology and the Swedish Research Council (VR 2018–041449). We acknowledge the Paul Scherrer Institute, Villigen, Switzerland for provision of synchrotron radiation beamtime at the beamline cSAXS of the SLS, and the Statistical Consulting Group at ETH Zurich for providing advice during the statistical image analysis. CA acknowledges the funding received from the European Union's Horizon 2020 research and innovation program under the Marie Sklodovska-Curie grant agreement No 884104. ZG acknowledges funding from the Swiss National Science Foundation (SNF), project number 200021_178788.

Appendix A. Supplementary data

Supplementary data to this article can be found online at https://doi.org/10.1016/j.biomaterials.2022.121989.

References

[1] E.H. Schemitsch, Size matters: defining critical in bone defect size, J. Orthop. Trauma 31 (Suppl 5) (2017) S20–S22.
[2] E. Roddy, M.R. DeBaun, A. Daoud-Gray, Y.P. Yang, M.J. Gardner, Treatment of critical-sized bone defects: clinical and tissue engineering perspectives, Eur. J. Orthop. Surg. Traumatol. 28 (3) (2018) 351–362.
[3] L. Audige, D. Griffin, M. Bhandari, J. Kellam, T.P. Ruedi, Path analysis of factors for delayed healing and nonunion in 416 operatively treated tibial shaft fractures, Clin. Orthop. Relat. Res. 438 (2005) 221–232.
[4] R. Dimitriou, E. Jones, D. McGonagle, P.V. Giannoudis, Bone regeneration: current concepts and future directions, BMC Med. 9 (2011) 66.
[5] P. Habibovic, (*) strategic directions in osteoinduction and biomimetics, Tissue Eng. 23 (23–24) (2017) 1295–1296.
[6] B. Baroli, From natural bone grafts to tissue engineering therapeutics: brainstorming on pharmaceutical formulative requirements and challenges, J. Pharmacol. Sci. 98 (4) (2009) 1317–1375.
[7] L. Roseti, V. Parisi, M. Petretta, C. Cavallo, G. Desando, I. Bartolotti, B. Grigolo, Scaffolds for bone tissue engineering: state of the art and new perspectives, Mater Sci Eng C Mater Biol Appl 78 (2017) 1246–1262.
[8] A.R. Amini, C.T. Laurencin, S.P. Nukavarapu, Bone tissue engineering: recent advances and challenges, Crit. Rev. Biomed. Eng. 40 (5) (2012) 363–408.
[9] J. Aronson, Limb-lengthening, skeletal reconstruction, and bone transport with the Ilizarov method, J Bone Joint Surg Am 79 (8) (1997) 1243–1258.
[10] S.A. Green, J.M. Jackson, D.M. Wall, H. Marinow, J. Ishkanian, Management of segmental defects by the Ilizarov intercalary bone transport method, Clin. Orthop. Relat. Res. 280 (1992) 136–142.
[11] P.V. Giannoudis, H. Dinopoulos, E. Tsiridis, Bone substitutes: an update, Injury 36 (Suppl 3) (2005) S20–S27.
[12] P.V. Giannoudis, T.A. Einhorn, Bone morphogenetic proteins in musculoskeletal medicine, Injury 40 (Suppl 3) (2009) S1–S3.
[13] T.W. Bauer, G.F. Muschler, Bone graft materials. An overview of the basic science, Clin. Orthop. Relat. Res. 371 (2000) 10–27.
[14] C.G. Finkemeier, Bone-grafting and bone-graft substitutes, J Bone Joint Surg Am 84 (3) (2002) 454–464.
[15] P. Hernigou, A. Poignard, O. Manicom, G. Mathieu, H. Rouard, The use of percutaneous autologous bone marrow transplantation in nonunion and avascular necrosis of bone, J Bone Joint Surg Br 87 (7) (2005) 896–902.
[16] J.S. Silber, D.G. Anderson, S.D. Daffner, B.T. Brislin, J.M. Leland, A.S. Hilibrand, A. R. Vaccaro, T.J. Albert, Donor site morbidity after anterior iliac crest bone harvest for single-level anterior cervical discectomy and fusion, Spine (Phila Pa 28 (2) (1976) 134–139, 2003.
[17] P.V. Giannoudis, T.A. Einhorn, D. Marsh, Fracture healing: the diamond concept, Injury 38 (Suppl 4) (2007) S3–S6.
[18] S. Bose, M. Roy, A. Bandyopadhyay, Recent advances in bone tissue engineering scaffolds, Trends Biotechnol. 30 (10) (2012) 546–554.
[19] E.L. Fong, B.M. Watson, F.K. Kasper, A.G. Mikos, Building bridges: leveraging interdisciplinary collaborations in the development of biomaterials to meet clinical needs, Adv. Mater. 24 (36) (2012) 4995–5013.
[20] B.B. Nguyen, R.A. Moriarty, T. Kamalitdinov, J.M. Etheridge, J.P. Fisher, Collagen hydrogel scaffold promotes mesenchymal stem cell and endothelial cell coculture for bone tissue engineering, J. Biomed. Mater. Res. 105 (4) (2017) 1123–1131.
[21] M.I. Santos, R.L. Reis, Vascularization in bone tissue engineering: physiology, current strategies, major hurdles and future challenges, Macromol. Biosci. 10 (1) (2010) 12–27.
[22] J. Wang, M. Yang, Y. Zhu, L. Wang, A.P. Tomsia, C. Mao, Phage nanofibers induce vascularized osteogenesis in 3D printed bone scaffolds, Adv. Mater. 26 (29) (2014) 4961–4966.
[23] C.N. Kelly, T. Wang, J. Crowley, D. Wills, M.H. Pelletier, E.R. Westrick, S.B. Adams, K. Gall, W.R. Walsh, High-strength, porous additively manufactured implants with optimized mechanical osseointegration, Biomaterials 279 (2021), 121206.
[24] Y. Liu, J. Fang, Q. Zhang, X. Zhang, Y. Cao, W. Chen, Z. Shao, S. Yang, D. Wu, M. Hung, Y. Zhang, W. Tong, H. Tian, Wnt10b-overexpressing umbilical cord

mesenchymal stem cells promote critical size rat calvarial defect healing by enhanced osteogenesis and VEGF-mediated angiogenesis, J Orthop Translat 23 (2020) 29–37.
[25] Y. Shi, R. He, X. Deng, Z. Shao, D. Deganello, C. Yan, Z. Xia, Ys, Xd Rh, Xd Rh, Dd Zs, Cy Dd, Cy Zx, Cy Zx, Ys Zx, Zx Zx, Three-dimensional biofabrication of an aragonite-enriched self-hardening bone graft substitute and assessment of its osteogenicity in vitro and in vivo, Biomater Transl 1 (1) (2020) 69–81.
[26] M.H. Ho, D.M. Wang, H.J. Hsieh, H.C. Liu, T.Y. Hsien, J.Y. Lai, L.T. Hou, Preparation and characterization of RGD-immobilized chitosan scaffolds, Biomaterials 26 (16) (2005) 3197–3206.
[27] W.J. Li, R. Tuli, X. Huang, P. Laquerriere, R.S. Tuan, Multilineage differentiation of human mesenchymal stem cells in a three-dimensional nanofibrous scaffold, Biomaterials 26 (25) (2005) 5158–5166.
[28] G. Wang, L. Zheng, H. Zhao, J. Miao, C. Sun, N. Ren, J. Wang, H. Liu, X. Tao, In vitro assessment of the differentiation potential of bone marrow-derived mesenchymal stem cells on genipin-chitosan conjugation scaffold with surface hydroxyapatite nanostructure for bone tissue engineering, Tissue Eng. 17 (9–10) (2011) 1341–1349.
[29] P. Yilgor, K. Tuzlakoglu, R.L. Reis, N. Hasirci, V. Hasirci, Incorporation of a sequential BMP-2/BMP-7 delivery system into chitosan-based scaffolds for bone tissue engineering, Biomaterials 30 (21) (2009) 3551–3559.
[30] R.A. Thibault, A.G. Mikos, F.K. Kasper, Scaffold/Extracellular matrix hybrid constructs for bone-tissue engineering, Adv Healthc Mater 2 (1) (2013) 13–24.
[31] L.F. Tapias, H.C. Ott, Decellularized scaffolds as a platform for bioengineered organs, Curr. Opin. Organ Transplant. 19 (2) (2014) 145–152.
[32] D.J. Lee, S. Diachina, Y.T. Lee, L. Zhao, R. Zou, N. Tang, H. Han, X. Chen, C.C. Ko, Decellularized bone matrix grafts for calvaria regeneration, J. Tissue Eng. 7 (2016), 2041731416680306.
[33] S. Bhumiratana, J.C. Bernhard, D.M. Alfi, K. Yeager, R.E. Eton, J. Bova, F. Shah, J. M. Gimble, M.J. Lopez, S.B. Eisig, G. Vunjak-Novakovic, Tissue-engineered autologous grafts for facial bone reconstruction, Sci. Transl. Med. 8 (343) (2016) 343ra83.
[34] V. Mourino, A.R. Boccaccini, Bone tissue engineering therapeutics: controlled drug delivery in three-dimensional scaffolds, J. R. Soc. Interface 7 (43) (2010) 209–227.
[35] P. Gentile, V. Chiono, I. Carmagnola, P.V. Hatton, An overview of poly(lactic-co-glycolic) acid (PLGA)-based biomaterials for bone tissue engineering, Int. J. Mol. Sci. 15 (3) (2014) 3640–3659.
[36] X. Liu, P.X. Ma, Polymeric scaffolds for bone tissue engineering, Ann. Biomed. Eng. 32 (3) (2004) 477–486.
[37] Z. Pan, J. Ding, Poly(lactide-co-glycolide) porous scaffolds for tissue engineering and regenerative medicine, Interface Focus 2 (3) (2012) 366–377.
[38] R. Vasita, D.S. Katti, Nanofibers and their applications in tissue engineering, Int. J. Nanomed. 1 (1) (2006) 15–30.
[39] W.J. Li, C.T. Laurencin, E.J. Caterson, R.S. Tuan, F.K. Ko, Electrospun nanofibrous structure: a novel scaffold for tissue engineering, J. Biomed. Mater. Res. 60 (4) (2002) 613–621.
[40] Z. Ma, M. Kotaki, R. Inai, S. Ramakrishna, Potential of nanofiber matrix as tissue-engineering scaffolds, Tissue Eng. 11 (1–2) (2005) 101–109.
[41] J.A. Matthews, G.E. Wnek, D.G. Simpson, G.L. Bowlin, Electrospinning of collagen nanofibers, Biomacromolecules 3 (2) (2002) 232–238.
[42] L.A. Smith, P.X. Ma, Nano-fibrous scaffolds for tissue engineering, Colloids Surf. B Biointerfaces 39 (3) (2004) 125–131.
[43] C.H. Lee, H.J. Shin, I.H. Cho, Y.M. Kang, I.A. Kim, K.D. Park, J.W. Shin, Nanofiber alignment and direction of mechanical strain affect the ECM production of human ACL fibroblast, Biomaterials 26 (11) (2005) 1261–1270.
[44] O. Groninger, S. Hess, D. Mohn, E. Schneider, W. Stark, S. Marsmann, P. Wolint, M. Calcagni, P. Cinelli, J. Buschmann, Directing stem cell commitment by amorphous calcium phosphate nanoparticles incorporated in PLGA: relevance of the free calcium ion concentration, Int. J. Mol. Sci. 21 (7) (2020).
[45] S.C. Hess, W.J. Stark, D. Mohn, N. Cohrs, S. Marsmann, M. Calcagni, P. Cinelli, J. Buschmann, Gene expression in human adipose-derived stem cells: comparison of 2D films, 3D electrospun meshes or co-cultured scaffolds with two-way paracrine effects, Eur. Cell. Mater. 34 (2017) 232–248.
[46] J. Jeong, J.H. Kim, J.H. Shim, N.S. Hwang, C.Y. Heo, Bioactive calcium phosphate materials and applications in bone regeneration, Biomater. Res. 23 (2019) 4.
[47] S. Samavedi, A.R. Whittington, A.S. Goldstein, Calcium phosphate ceramics in bone tissue engineering: a review of properties and their influence on cell behavior, Acta Biomater. 9 (9) (2013) 8037–8045.
[48] S. Gao, M. Calcagni, M. Welti, S. Hemmi, N. Hild, W.J. Stark, G.M. Burgisser, G. A. Wanner, P. Cinelli, J. Buschmann, Proliferation of ASC-derived endothelial cells in a 3D electrospun mesh: impact of bone-biomimetic nanocomposite and co-culture with ASC-derived osteoblasts, Injury 45 (6) (2014) 974–980.
[49] R. Dai, Z. Wang, R. Samanipour, K.I. Koo, K. Kim, Adipose-derived stem cells for tissue engineering and regenerative medicine applications, Stem Cell. Int. 2016 (2016), 6737345.
[50] J. Buschmann, L. Harter, S. Gao, S. Hemmi, M. Welti, N. Hild, O.D. Schneider, W. J. Stark, N. Lindenblatt, C.M. Werner, G.A. Wanner, M. Calcagni, Tissue engineered bone grafts based on biomimetic nanocomposite PLGA/amorphous calcium phosphate scaffold and human adipose-derived stem cells, Injury 43 (10) (2012) 1689–1697.
[51] P. Fratzl, S. Schreiber, K. Klaushofer, Bone mineralization as studied by small-angle x-ray scattering, Connect. Tissue Res. 34 (4) (1996) 247–254.
[52] S. Pabisch, W. Wagermaier, T. Zander, C. Li, P. Fratzl, Imaging the nanostructure of bone and dentin through small- and wide-angle X-ray scattering, Methods Enzymol. 532 (2013) 391–413.
[53] M. Georgiadis, M. Guizar-Sicairos, A. Zwahlen, A.J. Trüssel, O. Bunk, R. Müller, P. Schneider, 3D scanning SAXS: a novel method for the assessment of bone ultrastructure orientation, Bone 71 (2015) 42–52.
[54] M. Georgiadis, M. Guizar-Sicairos, O. Gschwend, P. Hangartner, O. Bunk, R. Müller, P. Schneider, Ultrastructure organization of human trabeculae assessed by 3D sSAXS and relation to bone microarchitecture, PLoS One 11 (8) (2016), e0159838.
[55] M. Liebi, M. Georgiadis, A. Menzel, P. Schneider, J. Kohlbrecher, O. Bunk, M. Guizar-Sicairos, Nanostructure surveys of macroscopic specimens by small-angle scattering tensor tomography, Nature 527 (7578) (2015) 349–352.
[56] M. Guizar-Sicairos, M. Georgiadis, M. Liebi, Validation study of small-angle X-ray scattering tensor tomography, J. Synchrotron Radiat. 27 (2020) 779–787.
[57] T.A. Grunewald, M. Liebi, N.K. Wittig, A. Johannes, T. Sikjaer, L. Rejnmark, Z. R. Gao, M. Rosenthal, M. Guizar-Sicairos, H. Birkedal, M. Burghammer, Mapping the 3D orientation of nanocrystals and nanostructures in human bone: indications of novel structural features, Sci. Adv. 6 (24) (2020).
[58] M. Liebi, V. Lutz-Bueno, M. Guizar-Sicairos, B.M. Schonbauer, J. Eichler, E. Martinelli, J.F. Loffler, A. Weinberg, H. Lichtenegger, T.A. Grunewald, 3D nanoscale analysis of bone healing around degrading Mg implants evaluated by X-ray scattering tensor tomography, Acta Biomater. 134 (2021) 804–817.
[59] M. Georgiadis, A. Schroeter, Z. Gao, M. Guizar-Sicairos, M. Liebi, C. Leuze, J. A. McNab, A. Balolia, J. Veraart, B. Ades-Aron, S. Kim, T. Shepherd, C.H. Lee, P. Walczak, S. Chodankar, P. DiGiacomo, G. David, M. Augath, V. Zerbi, S. Sommer, I. Rajkovic, T. Weiss, O. Bunk, L. Yang, J. Zhang, D.S. Novikov, M. Zeineh, E. Fieremans, M. Rudin, Nanostructure-specific X-ray tomography reveals myelin levels, integrity and axon orientations in mouse and human nervous tissue, Nat. Commun. 12 (1) (2021).
[60] S. Loher, W.J. Stark, M. Maciejewski, A. Baiker, S.E. Pratsinis, D. Reichardt, F. Maspero, F. Krumeich, D. Gunther, Fluoro-apatite and calcium phosphate nanoparticles by flame synthesis, Chem. Mater. 17 (1) (2005) 36–42.
[61] O.D. Schneider, S. Loher, T.J. Brunner, L. Uebersax, M. Simonet, R.N. Grass, H. P. Merkle, W.J. Stark, Cotton wool-like nanocomposite biomaterials prepared by electrospinning: in vitro bioactivity and osteogenic differentiation of human mesenchymal stem cells, J. Biomed. Mater. Res. B Appl. Biomater. 84 (2) (2008) 350–362.
[62] P.A. Zuk, M. Zhu, H. Mizuno, J. Huang, J.W. Futrell, A.J. Katz, P. Benhaim, H. P. Lorenz, M.H. Hedrick, Multilineage cells from human adipose tissue: implications for cell-based therapies, Tissue Eng. 7 (2) (2001) 211–228.
[63] M. Dominici, K. Le Blanc, I. Mueller, I. Slaper-Cortenbach, F. Marini, D. Krause, R. Deans, A. Keating, D. Prockop, E. Horwitz, Minimal criteria for defining multipotent mesenchymal stromal cells, The International Society for Cellular Therapy position statement, Cytotherapy 8 (4) (2006) 315–317.
[64] D.D. Canepa, E.A. Casanova, E. Arvaniti, V. Tosevski, S. Marsmann, B. Eggerschwiler, S. Halvachizadeh, J. Buschmann, A.A. Barth, J.A. Plock, M. Claassen, H.C. Pape, P. Cinelli, Identification of ALP+/CD73+ defining markers for enhanced osteogenic potential in human adipose-derived mesenchymal stromal cells by mass cytometry, Stem Cell Res. Ther. 12 (1) (2021) 7.
[65] K.J. Livak, T.D. Schmittgen, Analysis of relative gene expression data using real-time quantitative PCR and the 2(-Delta Delta C(T)) Method, Methods 25 (4) (2001) 402–408.
[66] R.W. Farndale, D.J. Buttle, A.J. Barrett, Improved quantitation and discrimination of sulphated glycosaminoglycans by use of dimethylmethylene blue, Biochim. Biophys. Acta 883 (2) (1986) 173–177.
[67] M. Manassero, V. Viateau, R. Matthys, M. Deschepper, R. Vallefuoco, M. Bensidhoum, H. Petite, A novel murine femoral segmental critical-sized defect model stabilized by plate osteosynthesis for bone tissue engineering purposes, Tissue Eng. C Methods 19 (4) (2013) 271–280.
[68] M. Liebi, M. Georgiadis, J. Kohlbrecher, M. Holler, J. Raabe, I. Usov, A. Menzel, P. Schneider, O. Bunk, M. Guizar-Sicairos, Small-angle X-ray scattering tensor tomography: model of the three-dimensional reciprocal-space map, reconstruction algorithm and angular sampling requirements, Acta Crystallographica Section A Foundations and Advances 74 (1) (2018) 12–24.
[69] B. Henrich, A. Bergamaschi, C. Broennimann, R. Dinapoli, E.F. Eikenberry, I. Johnson, M. Kobas, P. Kraft, A. Mozzanica, B. Schmitt, PILATUS: a single photon counting pixel detector for X-ray applications, Nucl. Instrum. Methods Phys. Res. Sect. A Accel. Spectrom. Detect. Assoc. Equip. 607 (1) (2009) 247–249.
[70] C.G. Schroer, M. Kuhlmann, S.V. Roth, R. Gehrke, N. Stribeck, A. Almendarez-Camarillo, B. Lengeler, Mapping the local nanostructure inside a specimen by tomographic small-angle x-ray scattering, Appl. Phys. Lett. 88 (16) (2006), 164102.
[71] P.S.I. CXS group, Scanning SAXS software package, Switzerland, https://www.psi.ch/en/sls/csaxs/software, 2019, https://www.psi.ch/en/sls/csaxs/software.
[72] O. Bunk, M. Bech, T.H. Jensen, R. Feidenhans'l, T. Binderup, A. Menzel, F. Pfeiffer, Multimodal x-ray scatter imaging, New J. Phys. 11 (12) (2009).
[73] M. Odstrčil, M. Holler, J. Raabe, M. Guizar-Sicairos, Alignment methods for nanotomography with deep subpixel accuracy, Opt Express 27 (25) (2019) 36637–36652.
[74] Z. Gao, M. Guizar-Sicairos, V. Lutz-Bueno, A. Schroter, M. Liebi, M. Rudin, M. Georgiadis, High-speed tensor tomography: iterative reconstruction tensor tomography (IRTT) algorithm, Acta Crystallogr. A 75 (2) (2019).
[75] P. Fratzl, N. Fratzl-Zelman, K. Klaushofer, G. Vogl, K. Koller, Nucleation and growth of mineral crystals in bone studied by small-angle X-ray scattering, Calcif. Tissue Int. 48 (6) (1991) 407–413.
[76] P. Fratzl, M. Groschner, G. Vogl, H. Plenk Jr., J. Eschberger, N. Fratzl-Zelman, K. Koller, K. Klaushofer, Mineral crystals in calcified tissues: a comparative study by SAXS, J. Bone Miner. Res. 7 (3) (1992) 329–334.

[77] T.J. Brunner, R.N. Grass, M. Bohner, W.J. Stark, Effect of particle size, crystal phase and crystallinity on the reactivity of tricalcium phosphate cements for bone reconstruction, J. Mater. Chem. 17 (38) (2007) 4072–4078.
[78] G.S. Hussey, J.L. Dziki, S.F. Badylak, Extracellular matrix-based materials for regenerative medicine, Nat. Rev. Mater. 3 (7) (2018) 159–173.
[79] R.M. Hoerth, B.M. Seidt, M. Shah, C. Schwarz, B.M. Willie, G.N. Duda, P. Fratzl, W. Wagermaier, Mechanical and structural properties of bone in non-critical and critical healing in rat, Acta Biomater. 10 (9) (2014) 4009–4019.
[80] L. Xi, Y. Zhang, H. Gupta, N. Terrill, P. Wang, T. Zhao, D. Fang, A multiscale study of structural and compositional changes in a natural nanocomposite: osteoporotic bone with chronic endogenous steroid excess, Bone 143 (2021), 115666.
[81] M. Artico, L. Ferrante, F.S. Pastore, E.O. Ramundo, D. Cantarelli, D. Scopelliti, G. Iannetti, Bone autografting of the calvaria and craniofacial skeleton: historical background, surgical results in a series of 15 patients, and review of the literature, Surg. Neurol. 60 (1) (2003) 71–79.
[82] S.N. Khan, J.F. Fraser, H.S. Sandhu, F.P. Cammisa Jr., F.P. Girardi, J.M. Lane, Use of osteopromotive growth factors, demineralized bone matrix, and ceramics to enhance spinal fusion, J. Am. Acad. Orthop. Surg. 13 (2) (2005) 129–137.
[83] Z. Li, M. Kawashita, Current progress in inorganic artificial biomaterials, J. Artif. Organs 14 (3) (2011) 163–170.
[84] Z. Ge, Z. Jin, T. Cao, Manufacture of degradable polymeric scaffolds for bone regeneration, Biomed. Mater. 3 (2) (2008), 022001.
[85] Y.S. Kim, M. Majid, A.J. Melchiorri, A.G. Mikos, Applications of decellularized extracellular matrix in bone and cartilage tissue engineering, Bioeng Transl Med 4 (1) (2019) 83–95.
[86] W. Baumgartner, L. Otto, S.C. Hess, W.J. Stark, S. Marsmann, G.M. Burgisser, M. Calcagni, P. Cinelli, J. Buschmann, Cartilage/bone interface fabricated under perfusion: spatially organized commitment of adipose-derived stem cells without medium supplementation, J. Biomed. Mater. Res. B Appl. Biomater. 107 (6) (2019) 1833–1843.
[87] W. Baumgartner, I. Schneider, S.C. Hess, W.J. Stark, S. Marsmann, M. Brunelli, M. Calcagni, P. Cinelli, J. Buschmann, Cyclic uniaxial compression of human stem cells seeded on a bone biomimetic nanocomposite decreases anti-osteogenic commitment evoked by shear stress, J. Mech. Behav. Biomed. Mater. 83 (2018) 84–93.
[88] J. Buschmann, E. Balli, S.C. Hess, W.J. Stark, P. Cinelli, S. Marsmann, M. Welti, W. Weder, W. Jungraithmayr, Effects of seeding adipose-derived stem cells on electrospun nanocomposite used as chest wall graft in a murine model, Injury 48 (10) (2017) 2080–2088.
[89] J. Buschmann, S. Gao, L. Harter, S. Hemmi, M. Welti, C.M. Werner, M. Calcagni, P. Cinelli, G.A. Wanner, Yield and proliferation rate of adipose-derived stromal cells as a function of age, body mass index and harvest site-increasing the yield by use of adherent and supernatant fractions? Cytotherapy 15 (9) (2013) 1098–1105.
[90] B. Eggerschwiler, D.D. Canepa, H.C. Pape, E.A. Casanova, P. Cinelli, Automated digital image quantification of histological staining for the analysis of the trilineage differentiation potential of mesenchymal stem cells, Stem Cell Res. Ther. 10 (1) (2019) 69.
[91] Y.C. Chai, S.J. Roberts, J. Schrooten, F.P. Luyten, Probing the osteoinductive effect of calcium phosphate by using an in vitro biomimetic model, Tissue Eng. 17 (7–8) (2011) 1083–1097.
[92] J. Rubin, C. Rubin, C.R. Jacobs, Molecular pathways mediating mechanical signaling in bone, Gene 367 (2006) 1–16.
[93] T. Albrektsson, C. Johansson, Osteoinduction, osteoconduction and osseointegration, Eur. Spine J. 10 (Suppl 2) (2001) S96–S101.
[94] D.A. Taylor, A.M. Chandler, A.S. Gobin, L.C. Sampaio, Maximizing cardiac repair: should we focus on the cells or on the matrix? Circ. Res. 120 (1) (2017) 30–32.
[95] D.A. Taylor, L.C. Sampaio, Z. Ferdous, A.S. Gobin, L.J. Taite, Decellularized matrices in regenerative medicine, Acta Biomater. 74 (2018) 74–89.
[96] M.A. Konig, D.D. Canepa, D. Cadosch, E. Casanova, M. Heinzelmann, D. Rittirsch, M. Plecko, S. Hemmi, H.P. Simmen, P. Cinelli, G.A. Wanner, Direct transplantation of native pericytes from adipose tissue: a new perspective to stimulate healing in critical size bone defects, Cytotherapy 18 (1) (2016) 41–52.
[97] R.M. Hoerth, M. Kerschnitzki, M. Aido, I. Schmidt, M. Burghammer, G.N. Duda, P. Fratzl, B.M. Willie, W. Wagermaier, Correlations between nanostructure and micromechanical properties of healing bone, J. Mech. Behav. Biomed. Mater. 77 (2018) 258–266.